DESIGN OF SUCTION ANCHORS IN SAND FOR WIND TURBINES

LUANA RIZZATO FERREIRA

Dissertation submitted in partial fulfilment of the requirements for the degree of

MASTER IN CIVIL ENGINEERING — SPECIALISATION IN STRUCTURES AND GEOTECHNICS

Supervisor: Professor Doctor Sara Rios da Rocha e Silva, PhD

Co-supervisor: Doctor Alessandra Rossati, PhD

JUNE, 2026

MASTER'S IN CIVIL ENGINEERING 2025/2026

DEPARTMENT OF CIVIL AND GEORESOURCES ENGINEERING

Tel. +351-22-508 1901

✉ m.ec@fe.up.pt

Edited by

FACULTY OF ENGINEERING OF THE UNIVERSITY OF PORTO

Rua Dr. Roberto Frias

4200-465 PORTO

Portugal

Tel. +351-22-508 1400

✉ feup@fe.up.pt

http://www.fe.up.pt

Dedicated to my parents

"O sucesso nasce do querer, da determinação e

da persistência em se chegar a um objetivo."

José de Alencar

ACKNOWLEDGEMENTS

I would like to express my sincere gratitude to my mother, who worked tirelessly to provide me the opportunities that have led me to this point, and who supported me throughout every stage of this journey, always offering unwavering support. I am also deeply grateful to my father, who inspired me to pursue a career in engineering and supported me throughout my academic path, playing a fundamental role in my achievements.

I would like to thank my fiancé for his continuous support and encouragement while I balanced my academic work, professional responsibilities, and our life together. He is the main reason I continue to persevere every day and never give up.

I would like to thank all my professors with whom I could learn a lot, specially my supervisor Professor Dra. Sara Rios, my co-supervisor Dra. Alessandra Rosati and Dr. Raffaele Cesaro that guided me through this journey. Also, I would like to thank TAILWIND project for allowing the utilization of their document data on this research.

I am also grateful to my friend Pedro, whom I had the pleasure of meeting at FEUP, for his support both academically and personally, and for his lasting friendship.

Finally, and above all, I would like to express my deepest gratitude to God, for His constant guidance and strength throughout this journey, and reminds me every day that no dream or plan is impossible for Him. Without Him, I would not be here.

ABSTRACT

Offshore wind energy has experienced a significant growth in recent years and boosted research for foundation solutions to support and stabilize the towers or floater structures. Suction caissons are a reliable, efficient and sustainable anchoring solution capable to resist to complex environmental and cyclic loading conditions.

This dissertation investigates the analytical designing solutions of suction caissons installed in sandy soils and subjected to tensile loads. The study focused on two distinct floating platform scenarios of TAILWIND project: a semi-submersible platform with semi-taut mooring lines and a TLP system with vertical tendons. The work evaluated existing methodologies initially designed for clays and their adaptations and challenges when applied to sands.

In a first stage, an overview of the available design solutions for offshore foundations and their particularities was reviewed. This included available analytical, empirical and numerical design methods for suction caissons under pure tensile loads, tensile inclined loads and cyclic loading. Moreover, TAILWIND deliverables were analysed to identify the geotechnical parameters of Reference location 2 associated to sandy soils.

The second stage involved the preliminary design of suction caissons based on tensile design loads and inclinations provided by TAILWIND project data to define the influence of the geometry, embedment depth and strength parameters in the tensile resistant capacities in static and cyclic conditions.

The results highlight the significant influence of each parameter on the overall behaviour and resistance of suction caissons installed in sandy soils. Analytical methods have some limitations but they provide a good bottom line for predesigning. This study also demonstrates the importance of considering soil-structure interactions and cyclic loading effects in the design stage of offshore suction anchors.

This study will provide an better understanding of the behaviour and design requirements for suction foundations for offshore renewable energy structures in Portugal shelf.

KEYWORDS: suction caissons, sandy soils, cyclic loading, tensile capacity, soil-structure interaction.

RESUMO

A energia eólica offshore experimentou um crescimento significativo nos últimos anos e impulsionou a pesquisa de soluções de fundação para suportar e estabilizar as torres ou estruturas flutuantes. Os caixões de sucção são uma solução de ancoragem confiável, eficiente e sustentável, capaz de resistir a condições ambientais complexas e cargas cíclicas.

Esta dissertação investiga as soluções analíticas de dimensionamento de caixões de sucção instalados em solos arenosos e sujeitos a cargas de tração. O estudo focou em dois cenários distintos de plataforma flutuante do projeto TAILWIND: uma plataforma semi-submersível com linhas de amarração semi-tensionadas e um sistema TLP com tendões verticais. O trabalho avaliou metodologias existentes, inicialmente projetadas para argilas, e suas adaptações e desafios quando aplicadas a areias.

Em uma primeira etapa, foi feita uma revisão geral das soluções de projeto disponíveis para fundações offshore e suas particularidades, incluindo métodos de projeto analíticos, empíricos e numéricos disponíveis para caixões de sucção sob cargas de tração verticais e inclinadas, e carregamento cíclico. Além disso, os ensaios do projeto TAILWIND foram analisados para identificar os parâmetros geotécnicos da localização de referência 2 associados a solos arenosos.

A segunda etapa envolveu o dimensionamento preliminar de caixões de sucção com base nas cargas de projeto e respectivas inclinações fornecidas pelo projeto TAILWIND para definir a influência da geometria, penetração e parâmetros do solo nas capacidades resistentes à tração em condições estáticas e cíclicas.

Os resultados destacam a influência significativa de cada parâmetro no comportamento geral e na resistência dos caixões de sucção instalados em solos arenosos. Os métodos têm algumas limitações, mas fornecem uma boa base para o pré-dimensionamento. Este estudo também demonstra a importância de considerar as interações solo-estrutura e os efeitos do carregamento cíclico no projeto de âncoras de sucção. Este estudo proporcionará uma melhor compreensão do comportamento e dos requisitos de projeto para caixões de sucção para fundação de estruturas de energia renovável offshore na plataforma continental portuguesa.

PALAVRAS-CHAVE: caixões de sucção, solos arenosos, carregamentos cíclicos, sistemas de amarração, interação solo-estrutura.

TABLE OF CONTENTS

LIST OF FIGURES

LIST OF TABLES

PPP

SYMBOLS, ACRONYMS AND ABBREVIATIONS

K – lateral earth pressure coefficient

K_0 – Rankine's coefficient of earth pressure at rest

K_p – Rankine coefficient of passive earth pressure

V_{ult} – ultimate vertical tensile capacity

H_{ult} – ultimate horizontal tensile capacity

H_0 – horizontal tensile capacity at padeye

Zp – Normalized padeye depth

$Z_{p\text{-}opt}$ – optimum normalized padeye depth

z – soil depth

h – penetration of the caisson skirt

s – pressure in the caisson

as – excess pore pressure at tip of the caisson

D – diameter of the caisson

L – skirt length of the caisson

λ – aspect ratio

W – caisson submerged self-weight

m – load-spreading parameter to account for vertical stress reduction in the soil outside the caisson

N – lateral capacity factor

τ_a, τ_{cy} –average and cyclic shear stresses

γ_a ,γ_{cy} – average and cyclic shear strain

1
INTRODUCTION

1.1 OFFSHORE WIND ENERGY

1.1.1 Context

Offshore installations have their origin in the oil and gas (O&G) industry in the mid-1940s, with the first structures installed in water depths of approximately 6 m around 1947. By the early 1970s, offshore developments had progressed to water depths of 50–100 m, and currently offshore installations are being constructed in water depths ranging from 500 to 1,500 m [1].

Offshore wind energy (OWT) has been rapidly expanding in Europe and Asia, offering a more sustainable alternative to fossil fuel–based energy sources and responding to the growing demand for sustainable engineering solutions and recent international climate agreements [2]. Wind turbines installed on offshore platforms aim to maximize the exploitation of higher and more stable marine wind velocities, converting kinetic energy into electrical energy. This energy is subsequently transmitted to shore through submarine power cables.

1.1.2 Advantages of offshore wind energy

The main advantages of offshore wind farm deployment include the availability of higher and more consistent wind resources, which enables increased energy generation capacity and improved turbine efficiency. In addition, offshore installations have lower visual and acoustic impacts when compared to onshore wind farms, while allowing for the efficient use of maritime space. Offshore environments also offer substantial potential for large-scale expansion, supporting the development of utility-scale renewable energy projects [2].

1.1.3 Main challenges

Implementation costs have shown a decreasing trend in recent years; however, they still represent a challenging scenario, particularly regarding the construction of large offshore platforms in deep waters (approximately 500 m) and ultra-deep waters (up to 1,500 m) [3].

Installation and maintenance activities can be demanding, as they require a high level of technical expertise from construction and maintenance teams. The marine environment is more aggressive to structural components, requiring special corrosion protection systems, specialized maintenance workers, and increased caution and technical capability from both designers and construction teams during the design and execution of foundations. In addition, careful consideration must be given to the dynamic factors characteristic of the offshore environment, along with the requirement for specific safety certifications for personnel involved in offshore operations [4].

The selection of an appropriate foundation system for offshore installations is a fundamental aspect of overall project success, as it has significant financial and structural implications. Foundations may account for approximately 16–34% of the total project cost, depending on the size and location of the wind farm, and they also play a critical role in ensuring structural stability due to their dynamic sensitivity [2].

1.2 MAIN AND SPECIFIC OBJECTIVES

1.2.1 General objective

The general objective of this dissertation is to analyze existing analytical design methodologi.es for suction anchors evaluating their applicability in sandy soils, building upon existing and widely used design approaches originally formulated for clayey soils.

The study focuses on two distinct offshore scenarios: a semi-submersible platform supported by semi-taut mooring lines, and a tension leg platform (TLP) anchored by vertical mooring lines. By analyzing these two configurations, the dissertation seeks to assess the influence of different loading conditions and mooring systems on the geotechnical performance and design requirements of suction anchors.

1.2.2 Specific objectives

The specific objectives of this work are to:

- understand the soil–structure interaction governing the behavior of suction anchors installed in sandy soils.
- evaluate the anchor response under different loading conditions associated with distinct offshore mooring configurations.
- assess the design requirements and overall performance of suction anchors.

1.3 DOCUMENT STRUCTURE

This work is divided into two main parts. The first part consists of a critical review of existing analytical design methods for suction anchors, including an assessment of the applicability of installation and load capacity design approaches to sandy soils. This part also discusses the advantages and limitations of suction anchor systems, as well as the use of shared anchors in offshore applications.

The second part focuses on the preliminary design of suction anchors in sandy soil using data from the European project TAILWIND. In particular, the mooring line forces and their corresponding angles with respect to the horizontal, calculated for the two offshore scenarios previously described, are employed as input for the anchor design analyses.

2
LITERATURE REVIEW

2.1 Offshore environment

2.1.1 Offshore topography

Oceanic topography is composed of the continental shelf, continental rise, and the abyssal plain of the deep ocean. The distances between the continental shelf and the deep ocean vary according to the region and the continent. Figure 2-1presents a schematic representation of marine topography while Figure 2-2 presents a comparison of typical marine topographic profiles in different regions.

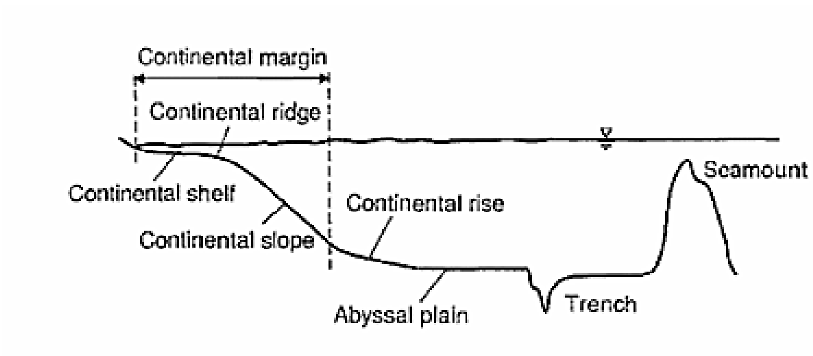

Figure 2-1. Ocean topography (after Poulos 1988)

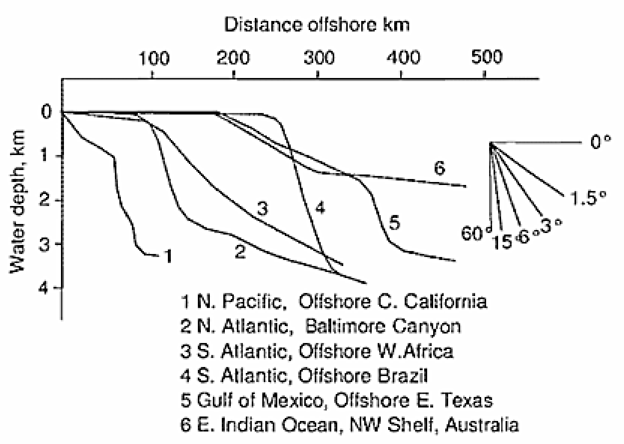

Figure 2-2. Offshore topography profile in different regions [2].

The continental shelf typically presents water depths ranging from 10 to 500 m, being deeper in glacial regions and shallower in coral reef areas. Beyond the edge of the continental shelf, water depths can reach between 2000 and 3000 m, with slopes exhibiting gradients ranging from 1:1000 to 1:700. The abyssal plain is characterized by a gentler gradient and reaches depths between 2500 and 6000 m [1].

In Portugal, the continental platform is composed by sandy sediments of a deformed carbonated sandstone, a well-graded sandy gravel layer up to 8m thick and a modern sandy deposit up to 7m thick, with effective friction angles in a range from 39º to 44º and deformation moduli between 22MPa and 54MPa [24].

An accurate site investigation is necessary to provide sufficient knowledge information about the parameters of the soil to make an optimum design of the foundation and mitigate possible structural problems and errors of design [24]. Portugal is having a good evolution in geotechnical research to build datasets that could be used to boost the offshore renewable energy of Portugal shelf.

2.1.2 Geotechnical aspects

Marine sediments are composed of debris originating either from the Earth's surface or from marine organisms and are generally classified as terrigenous or pelagic. Terrigenous materials are transported to the ocean by rivers, coastal erosion, glacial activity, or wind, and are classified according to particle size. Pelagic sediments, on the other hand, result from the decomposition of marine organisms and oceanic rocks and are typically fine-grained materials such as clays. Marine sediments may be also formed through biological and chemical reactions within the water column and are then classified as hydrogenous sediments [25].

The stress state of marine soils is defined according to their consolidation condition. Slowly deposited sediments are generally considered normally consolidated, although they may become slightly overconsolidated when subjected to glacial activity, unloading due to submarine landslides, gradual marine erosion, or past wave action increasing the effective stress between particles. Incompletely consolidated materials are associated with the incomplete dissipation of pore water pressures, typically resulting from rapid deposition, submarine sliding, gas dissociation, or cyclic wave loading [1].

The combined effect of these processes leads to significant spatial variability in soil formation across different regions. In the Gulf of Mexico, for example, soils are typically soft, normally consolidated, and composed of medium- to highly plastic clays with interbedded sand layers. In Brazil, soils are composed of clays and sands rich in carbonates. In West Africa, soil is generally soft and normally consolidated, with very stiff clay layers formed by rapid sediment deposition. In the North Sea and other glaciated regions, soils are stiff, consisting of overconsolidated clays and dense sands. In northeastern Australia, soils include carbonate sands, silts, and clays with varying degrees of cementation.

2.1.3 Hydrodynamic aspects

Offshore structures are subjected to a combination of meteorological and oceanographic actions (metocean conditions [7]), including:

- Surface wind;
- Wind-generated waves;
- Swell (long-period waves) generated by distant storms;

- Storm-induced currents;
- Deep-water currents associated with low-frequency circulation in large ocean basins;
- Local currents unrelated to storm events;
- In some regions, seismic activity and tsunamis.

The main oceanographic properties to be considered in the design of offshore structures are water density and viscosity. Salinity primarily influences water density and is considered a secondary parameter in most analyses, with greater variability observed near coastal areas. Temperature plays a key role in determining both density and viscosity, having an inverse relationship with these properties; that is, lower temperatures correspond to higher density and viscosity. Variations in water density with depth also contribute to the generation of internal waves in deep-water regions [7].

Another fundamental hydrodynamic aspect in the design and analysis of offshore structures is wave action. Waves are highly variable in terms of shape, period, velocity, and height, resulting in different loading effects on structures. In engineering practice, wave theory is typically applied to larger waves, which may be approximated to regular waves for design purposes.

2.1.4 Dynamic actions on offshore wind turbines

Offshore wind turbines are subjected not only to the previously described hydrodynamic actions but also to loads generated by wind interactions with the turbine blades. In addition, they are affected by aerodynamic rotor vibrations and blade passing loads, which contribute significantly to the overall dynamic response of the structure.

2.2 TYPES OF OFFSHORE FOUNDATIONS

2.2.1 Introduction

The foundations of offshore structures are among the most critical aspects of offshore wind system structural design, as they are responsible for ensuring the overall stability of the system and often play a decisive role in the economic feasibility of the project. The selection of an appropriate foundation type must consider factors such as installation challenges under varying meteorological conditions, seabed variability, required installation equipment, and compliance with local regulations [2].

Offshore substructures can generally be classified into two main groups, as illustrated in Figure 2-3 and Figure 2-4: fixed structures, in which the structure is directly supported by the seabed; and floating structures anchored to the seabed by mooring lines.

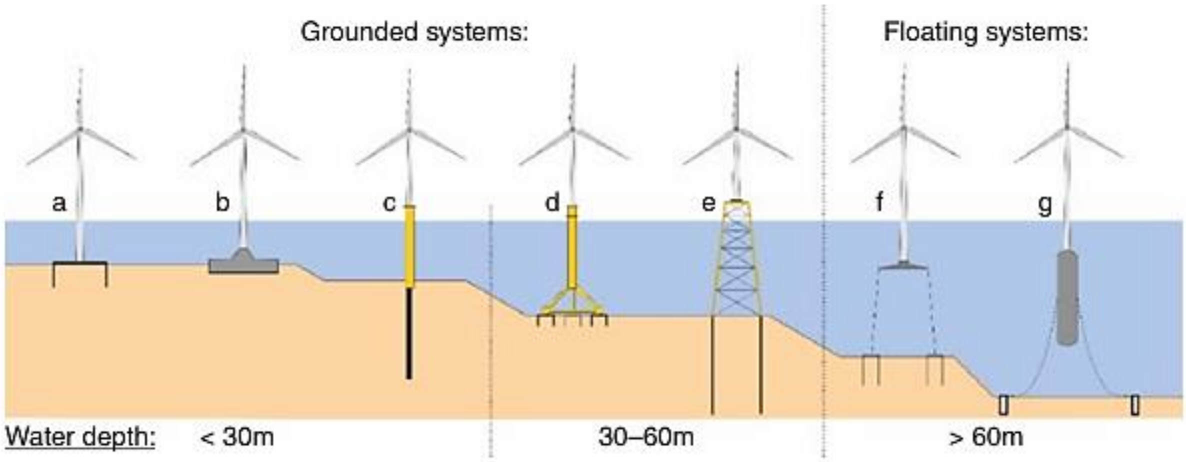

Figure 2-3. a) suction caisson; b) gravity-based; c) monopile; d) tripod on suction caisson; e) lattice structure; f) tension leg platform; g) spar buoy floating concept [2].

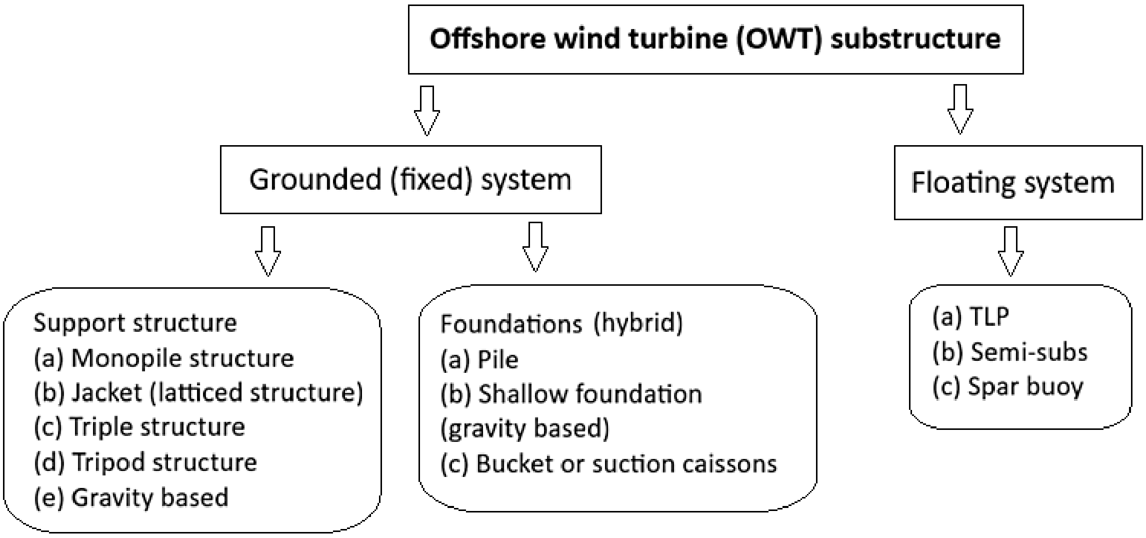

Figure 2-4. Flowchart for the classification of substructures (adapted from Bhattacharya [2])

Fixed offshore structures have their foundations directly into the seabed and may consist of shallow, deep, or hybrid foundation systems. As shown in Figure 2-4, shallow foundations are commonly used for fixed structures, while deep foundations can be used for fixed or floating structures. The load-bearing capacity of such foundations is determined through soil failure analyses and verification of mobilized shear resistance along the foundation–soil interface. The key design verifications include soil bearing capacity, friction in the walls and structural failure, ensuring that the applied loads remain below the corresponding resistances.

These foundations need to resist tensile and compressive loads. The main challenges for floating platforms are the dynamic resistance, logistics and installation, the maintenance and monitoring, and power transmission during movement of the cables

2.2.2 Tension leg platform

Tension Leg Platforms (TLP) are floating structures vertically anchored to the seabed by means of tensioned tendons or steel cables. The anchoring foundations are primarily designed to resist tensile loads.

2.2.3 Semi-submersible platforms

Semi-submersible systems rely on buoyancy to achieve static stability. Stability is obtained by shifting the centre of buoyancy within the submerged volume, while the centre of gravity of the structure remains fixed, generating a restoring moment when subjected to external displacements.

2.2.4 Spar buoy

The spar buoy is a ballast-stabilized system based on Archimedes' principle. The structure consists of a steel cylinder partially filled with ballast materials such as rock or water, lowering the centre of gravity below the centre of buoyancy. This configuration generates a restoring force opposing external loads.

All floating platforms need to be anchored to the seabed by means of different types of anchors such as piles, suction anchors, or other types of anchors.

2.2.5 Gravity-based foundations (fixed)

Gravity-based structures are shallow foundations designed to resist buoyancy and overturning due to their deadweight, preventing tensile stresses between the supporting structure and the seabed. Load equilibrium is achieved through the combined permanent loads of the foundation and the superstructure. When these loads are insufficient, additional ballast such as rock, steel, or concrete is used to increase the self-weight of the foundation.

The installation of gravity-based foundations requires seabed preparation to prevent any inclination. These foundations may be constructed in situ or using prefabricated concrete units, which are transported to the installation site by vessels and installed with or without crane assistance [2].

2.2.6 Pile foundations (fixed and floating)

Pile foundations are deep foundations that transfer loads through a combination of shaft friction and end-bearing resistance. These piles may act individually or as part of pile groups and are typically installed by driving tubular steel piles into the seabed using hydraulic hammers, generating vibrations and noise.

Monopiles are large-diameter steel piles, typically ranging from 3 m to 7 m in diameter, driven into the seabed. This is the most used foundation type for offshore wind turbines and is generally applied in water depths up to 25–30 m, with penetration depths ranging from 25 to 40 m [2].

2.2.7 Suction anchors (fixed and floating)

Suction anchors are hybrid foundations, exhibiting characteristics of both shallow and deep foundations. They consist of a cylindrical structure open at the base and sealed at the top. Their diameter-to-depth ratio makes them too deep to be classified as shallow foundations, yet not deep enough to be considered conventional deep foundations.

Suction anchors act as tension anchors capable of resisting vertical and inclined loads. Due to their hybrid nature, their resistance depends on both the soil bearing capacity and the shaft friction developed along the soil–structure interface [2].

2.2.7.1 Installation in clays vs sands

The installation of suction caissons occurs in two stages: gravity penetration and application of internal suction. These stages are illustrated in Figure 2-5.

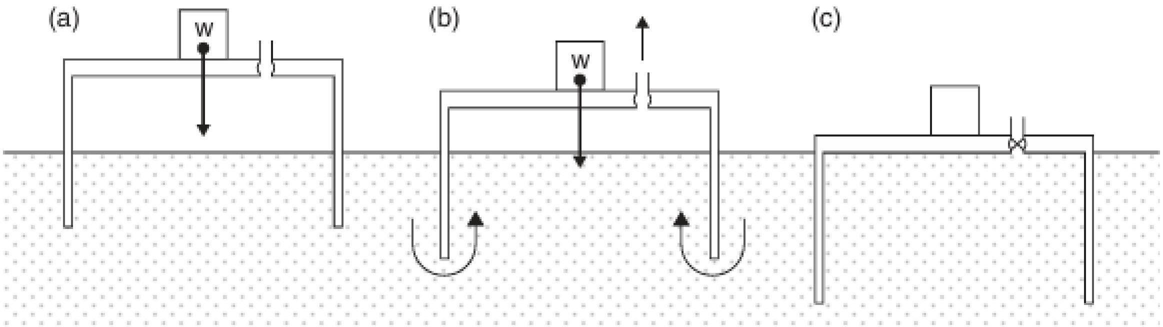

Figure 2-5 Installation stages of suction caissons: (a) gravity penetration; (b) application of internal suction; (c) completed installation [2] [13].

Depending on soil types, the installation requires careful analysis due to their distinct behaviours. Clays exhibits low permeability and can maintain high suction levels throughout installation without the need for drainage. In contrast, sands dissipate suction rapidly, requiring careful control of internal pressures.

The main challenges associated with installation in sandy soil include:

Risk of upward seepage flow.

Loss of lateral support due to localized liquefaction.

Difficulty in adapting to an inclined seabed.

Reduced soil–caisson resistance.

2.3 OTHER DESIGN CONSTRAINS

2.3.1 Shared anchors and mooring systems

Shared anchors refer to systems in which two or more floating structures are connected to a single anchor, forming a shared foundation system. This approach can reduce installation costs and carbon footprint [14]. However, it may increase the load demand on the anchor and introduce more complex interaction mechanisms, potentially leading to cascading failures affecting multiple floating structures [3]

2.3.2 Available design methods

Available calculation methods can be grouped into three main approaches:

- Analytical limit equilibrium methods.
- Semi-empirical methods based on, centrifuge tests results, or numerical analysis.
- Numerical methods using finite element analysis.

Each approach plays a specific role in offshore foundation design. Analytical methods like Houlsby et al. [13] are essential for preliminary design and safety factors assessment. In situ tests, such as CPT, are particularly important for sandy or heterogeneous soils due to the importance of site geotechnical knowledge of the seabed to mitigate errors in the design or structural failure. Semi-empirical methods as Zhao et al. [16] and Hirai [18] provide mathematical solutions for designing suction caissons validated with centrifuge tests. Numerical methods allow for a more refined modelling of foundation behaviour and offshore wind structures, enabling the simulation of complex interactions between floating systems and dynamic loading conditions.

These foundation systems require advanced numerical modelling to capture the combination of factors that may lead to failure. Design approaches may include degradation models, simplified macro-models (0D), one-dimensional models (1D), and advanced three-dimensional finite element models (3D). [3]

2.3.3 Standards and technical guidelines

There are some institutions that produce standards, guidelines and technical specifications for the design, installation, and performance of offshore structures. The main institutions are DNV (Det Norske Veritas) - a Norwegian society which establishes safety, reliability and performance standards for platforms, ships, pipelines and energy infrastructure, API (American Petroleum Institute) - a commercial association that establishes the main standards for equipment and maritime works, ABNT (Associação Brasileira de Normas Técnicas) that establishes standards for design and performance of structures and materials in Brazil, ISO (International Organization for Standardization), that establishes standards for safety operations in offshore structures for petroleum and gas, and Petrobras which is a Brazilian company involved in offshore structures for oil and gas that develops security standards for offshore works.

Among the main international standards:

- DNVGL-RP-C212 – Offshore Soil Mechanics
- DNV-ST-0119 – Floating Wind Turbine Structures
- ISO 19901-4 – Geotechnical and Foundation Design
- API RP 2GEO – Geotechnical Design Considerations

Among Brazilian standards and guidelines:

- ABNT NBR 15346 – Offshore structural design
- Petrobras N-1710 – Mooring systems
- Petrobras N-1706/N-1707 – Offshore structures and geotechnics

This research focused on applying analytical and semi-empirical (section 2.5) approaches to designing and then applying the safety factors of DNV [19] standards to understand the behaviour of a suction caisson under tensile forces.

2.4 EMPIRICAL METHODS FOR SUCTION CAISSON DESIGN

2.4.1 Vertical capacity under tensile load

For the vertical uplift capacity of the caisson, three approaches were analyzed to verify the similarities and differences between them and how they are used to design suction caissons. Most of the approaches are based on Houlsby et al. [13] initial assumptions and further extended considering centrifuge tests or numerical approaches. For this reason, Houlsby et al. [13] approach will be the first to be presented.

2.4.1.1 Houlsby et al. approach

On Houlsby et al. [13] proposal for suction caissons, the vertical uplift capacity is the sum of the internal and external frictional resistance as identified in equation (2-1), not considering the reduction of the vertical stress close to the caisson.

$$V_{ult} = -\frac{\gamma' h^2}{2}(Ktan\delta)_o(\pi D)_o - \frac{\gamma' h^2}{2}(Ktan\delta)_i(\pi D)_i \qquad \text{(2-1)}$$

where the Do and Di are the external and internal diameters as in

Figure 2-6 and Figure 2-7, γ' is the effective weight of the soil, V_{ult} is the ultimate uplift capacity, h is the penetration depth, K is the lateral pressure coefficient, and δ is the soil-interface frictional angle. These two latter variables never appear separately.

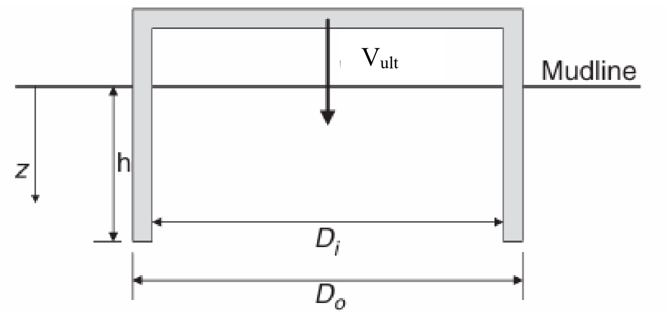

Figure 2-6. Caisson geometry

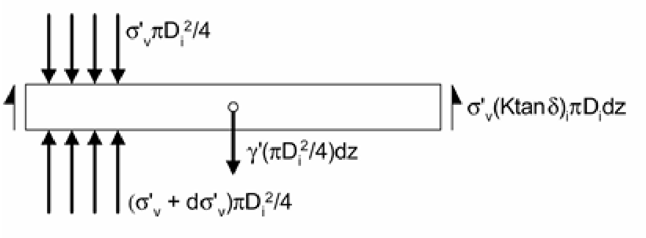

Figure 2-7. Vertical equilibrium of a slice of soil within the caisson (Houlsby et al. [13])

A verification must be made that the friction inside the caisson does not exceed the weight of the soil plug given by γ' h π $D_i^2/4$.

Under rapid tensile loading, a suction caisson in sand has a limiting uplift capacity given by the suction developed inside the caisson, and friction on the outer wall. There are many different possible modes of failure and Houlsby et al. [13] developed simple calculations to determine the capacities under various scenarios.

If the tensile load is applied very slowly, then pore pressure will be small, so drained conditions can be assumed. In tensile loading the annular rim is so small that can be neglected. The frictional terms are calculated for the installation scenario, where the shear stress acting on the caisson is σ'_v K tan δ.

Neglecting the reduction of stress close to the caisson leads to an overestimation of the force that can be developed, so Houlsby et al. [13] developed a theory to take this effect into account. Considering the reduction of vertical stress due to the action of upward friction from the caisson in a zone between diameters D_o and D_m=m D_o, where m is a multiple of the diameter over which vertical stress is enhanced, and assuming that there's no shear stress on vertical planes at diameter D_m, the same results as for the inside of the caisson are obtained, but with Zi (eq. (2-2)) replaced by.

$$Z_i = \frac{D_i}{4(Ktan\delta)} \tag{2-2}$$

Accounting for the effects of stress enhancement, the vertical tensile capacity in a special case where m is taken as a constant and uniform stress, for a penetration depth h, and already considering the soil plug effect, the equation (2-1) can be written as equation (2-3)

$$V_{ult} = -\gamma\, Z_o^2 y\left(\frac{h}{Z_o}\right)(Ktan\delta)_o(\pi D_o) - \gamma\, Z_i^2 y\left(\frac{h}{Z_i}\right)(Ktan\delta)_i(\pi D_i) \tag{2-3}$$

If the caisson is extracted more rapidly, then transient pore pressure will occur, and the suction within the caisson will need to be considered. The absolute pressure in the caisson is an average downward hydraulic gradient of the excess pore pressure at tip of the caisson divided by the vertical stress of water ($\frac{as}{\gamma_w h}$) on the outside of the caisson and the upward hydraulic gradient of $\frac{(1-as)s}{\gamma_w h}$ on the inside. The absolute pore pressure can then be rearranged as $pa + \gamma_w(h_w + h) - as$, where pa is the atmospheric pressure, γ_w is the specific weight of the water, h_w is the water depth and as is the excess pore pressure at the tip of the caisson.

Assuming that the distribution of pore pressure on the inside and outside of the caisson is linear with depth, the solutions for the vertical stresses are exactly as before, except that γ' is replaced by γ'+as/h outside and by γ'-(1-4)s/h inside the caisson. Then the uplift capacity accounting for the differential pressure across the top and the pore pressure on the rim (for thick caisson) is calculated as eq. (2-4).

$$\begin{aligned} V_{ult} + s\left(\frac{\pi D_i^2}{4}\right) + as\left(\frac{\pi(D_o^2 - D_i^2)}{4}\right) \\ = \int_0^h \sigma'_{vo} dz (Ktan\delta)_o(\pi D_o) + \int_0^h \sigma'_{vi} dz (Ktan\delta)_i(\pi D_i) \end{aligned} \tag{2-4}$$

In special cases when m is constant and a uniform stress is assumed, the equation (2-4) is rewritten as equation (2-5).

$$\begin{aligned} V_{ult} + s\left(\frac{\pi D_i^2}{4}\right) + as\left(\frac{\pi(D_o^2 - D_i^2)}{4}\right) \\ = -\left(\gamma' + \frac{as}{h}\right) Z_o^2 y\left(\frac{h}{Z_o}\right)(Ktan\delta)_o(\pi D_o) \\ -\left(\gamma' - \frac{(1-a)s}{h}\right) Z_i^2 y\left(\frac{h}{Z_i}\right)(Ktan\delta)_i(\pi D_i) \end{aligned} \tag{2-5}$$

If the suction is sufficiently large that the soil within the caisson liquefies and γ’-(1-a)s/h=0, then almost all suction appears at the caisson tip. This means that the suction a≈1 , the above rearranges to γ’+as/h=s/h. Then equation (2-5) can be simplified to,

$$V_{ult} + s\left(\frac{\pi D_i^2}{4}\right) + as\left(\frac{\pi(D_o^2 - D_i^2)}{4}\right) = -\left(\frac{s}{h}\right)Z_o^2 y\left(\frac{h}{Z_o}\right)(Ktan\delta)_o(\pi D_o) \qquad \text{(2-6)}$$

For small thickness of the caisson, Do=Di=D=external diameter and the caisson area become A=πD²/4. In this case, the uplift vertical capacity becomes equation (2-7).

$$V_{ult} = -\left(\frac{s}{h}\right)Z^2 y\left(\frac{h}{Z}\right)(Ktan\delta)(\pi D) - sA = -sA\left(1 + \left(\frac{4Z^2}{Dh}\right)y\left(\frac{h}{Z}\right)(Ktan\delta)\right) \qquad \text{(2-7)}$$

Neglecting the effect of stress reduction would give equation (2-8).

$$V_{ult} = -sA\left(1 + \left(\frac{2h}{D}\right)(Ktan\delta)\right) \qquad \text{(2-8)}$$

In this case, the capacity is simply calculated by applying a linearly varying factor to the suction force beneath the lid.

2.4.1.2 Hirai approach

Hirai [17] analyses the effect of vertical tensile, lateral, and moment load on the ultimate capacity of suction caissons in sand using an analytical approach that comes from traditional bearing capacity theory. Hirai [17] compares his deformation-load responses of suction caissons for various embedment ratios in sand with laboratory test results to calibrate the approach.

The vertical uplift capacity after installation is evaluated considering a suction caisson in a nonhomogeneous sand with geometry and discretization as illustrated in Figure 2-8.

For a suction caisson in sand, subjected to a vertical tensile load under drained conditions, ultimate tensile capacity is expressed by Hirai [17] as the sum of the pullout friction inside the skirt wall, plus the soil plug contribution, plus the pullout friction outside the skirt, and plus the buoyant weight of the caisson, as shown is equation (2-9).

$$V_{ult} = \frac{\gamma'\pi D_i^3(e^{\mu L-1})}{(16K_s tan\delta)} + \frac{\gamma'^{D_i^2}L}{4} + 0.5\gamma'\pi D_e L^2 Ktan\delta + W \qquad \text{(2-9)}$$

Where V_{ult} is the ultimate tensile capacity of the suction caisson under drained conditions, K is the coefficient of lateral pressure and W is the buoyant weight of the caisson.

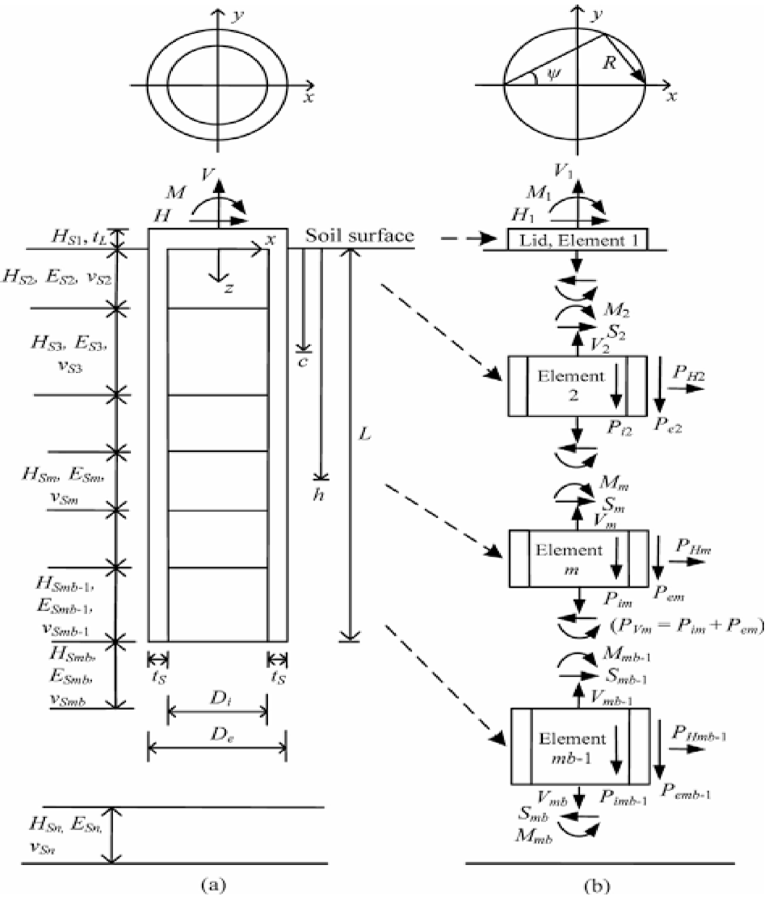

Figure 2-8 - a) Suction caisson and b) discretization of nonhomogeneous soil under tensile, lateral and moment loads (Hirai [17]).

2.4.1.3 Chenggen et al. approach

Chenggen et al. [18] adopts the SANISAND constitutive model to study the uplift responses of the caisson considering the influence of stress state on soil mechanical responses. The method is validated by comparison with centrifuge tests and preceding studies.

After developing the finite element model, Chenggen et al. [18] results showed that during the uplift progress of the caisson, the pore pressure accumulates, forming a seepage field in the soil. As higher the permeability of the soil less pressure beneath the caisson lid is accumulated.

The differential pressure equation must consider the effects of the pullout velocity, the aspect ratio and the frictional parameter Ktanδ. The final equation of the differential pressure p to consider all those parameters is given in equation (2-10).

$$p = f\left(\frac{v}{k}\right) g\left(\frac{L}{D}\right) j(K,\delta)\, \gamma_w D \qquad (2\text{-}10)$$

Where the first component is due to the pullout velocity (eq. (2-11)), the second component is due to the aspect ratio that may influence directly in the differential pressure (eq. (2-12)), the third component is because of Ktanδ. As the effect of friction coefficient on seepage is neglectable, it can be considered j(K,δ)=1.

$$f\left(\frac{v}{k}\right) = \begin{cases} e^{8.61\tanh\left(0.3\lg\frac{v}{k}+0.87\right)-6.07}, v/k \leq 10^4 \\ e^{2.5\tanh\left(0.43\lg\frac{v}{k}-0.09\right)-0.025}, v/k > 10^4 \end{cases} \qquad (2\text{-}11)$$

$$g\left(\frac{L}{D}\right) = \begin{cases} 1, & v/k \leq 10^{-1} \\ 0.236L/D + 0.764, & 10^{-1} < v/k \leq 10^4 \\ 0.212L/D + 0.788, & 10^4 < v/k \end{cases} \qquad (2\text{-}12)$$

As the pullout velocity increases, the differential pressure gradually accumulates, and soil plug expands. Neglecting the interaction between caisson and soil plug the caisson capacity is composed by the friction resistance outside the wall, the weight of the caisson plus the weight of the plug and the bottom force. This overall mechanism may be divided into two modules: soil plug and caisson (Figure 2-9).

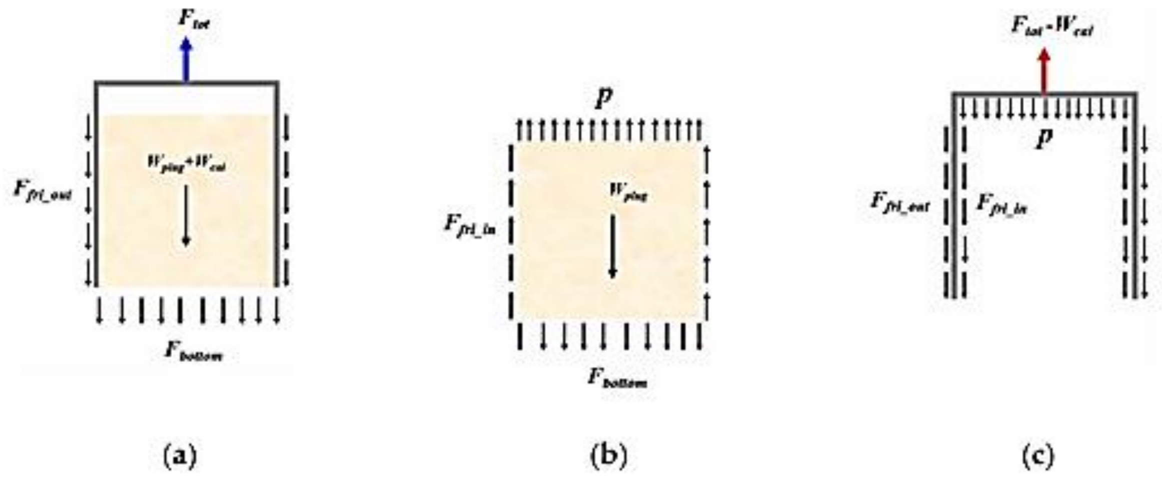

Figure 2-9 Bearing capacity mechanism a) overall bearing mode; b) soil plug module; and c) suction caisson module (Chenggen et al. [18]).

The force modes of the two modules can be expressed as in equations (2-13) and (2-14).

$$p\,\pi\frac{D_i^2}{4} + F_{fri,in} = W_{plug} + F_{bottom} \tag{2-13}$$

$$V_{ult} = F_{tot} - W = p\,\pi\frac{D_i^2}{4} + F_{fri,in} + F_{fri,out} \tag{2-14}$$

Where p is the differential pressure beneath the lid (eq. (2-10)), V_{ult} is the vertical force, Ftot is the total vertical force and W is the weight of the caisson. The frictional components for inside and outside the skirt wall is a function of the vertical effective stress of the soil and the frictional parameter Ktanδ as expressed in equations (2-15) and (2-16).

$$F_{fri,in} = \int_0^L \sigma_v' dz\ (Ktan\delta)_i(\pi D_i) \tag{2-15}$$

$$F_{fri,out} = \int_0^L \sigma_v' dz\ (Ktan\delta)_o(\pi D_o) \tag{2-16}$$

Since the differential pressure may contribute to the uplift capacity of the suction caisson, the pullout capacity might be normalized by the fully drained capacity that has its uplift capacity mainly due to the friction inside and outside as suggested by Houlsby et al. [13] (Figure 2-10). As the pullout velocity increases, the differential pressure accumulates beneath the lid and the uplift capacity can reach 10 times or more the fully drained resistance. Therefore, DNV [19] says that if the drainage mechanism of soil stratigraphy cannot be determined with confidence the design of suction must be conservative by adopting conservative assumptions.

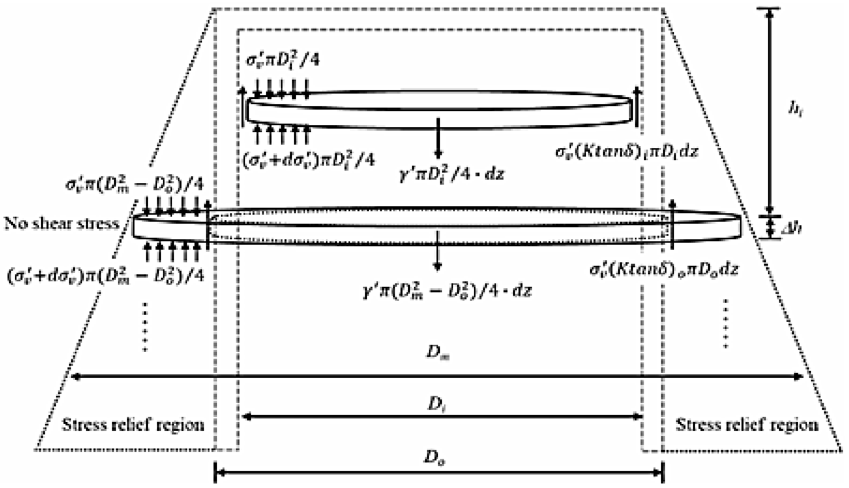

Figure 2-10 Soil effective stress along the caisson diameter at different depths (Chenggen et al. [18])

For uplift capacity in sands two cases need to be considered for tensile loading: slow (fully drained) loading and rapid (undrained) loading. In undrained conditions, the soil effective stress is enhanced by seepage, but the large pore pressure in the caisson may lead to soil liquefaction. Assuming that the increase in the outer skirt friction due to seepage force is proportional to the decrease on the inside, the uplift capacity can be expressed as equation (2-17).

$$V_{ult} = p\frac{\pi\, D_i^2}{4} + \frac{\gamma' h^2}{2}\left[(Ktan\delta)_i(\pi D_i) + (Ktan\delta)_o(\pi D_o)\right] \tag{2-17}$$

which can be simplified as equation (2-18).

$$V_{ult} = p\ \frac{\pi\, D_i^2}{4} + 2\,\pi\, D\frac{\gamma' h^2}{2}\ Ktan\delta \tag{2-18}$$

2.4.1.4 Comparison between vertical capacity approaches

Both Hirai [17] and Chenggen et al. [18] have their methodologies mainly based on Houlsby et al. [13] principle. To evaluate the differences of all those approaches to estimate the vertical tensile capacity a comparison of the resisting vertical capacity was taken by calculating a caisson with diameter Do=10m, Ktanδ=0.35 and a homogeneous soil.

The plotted graph presents the comparison of the tensile capacity obtained by the three described methodologies for several aspect ratios (λ=L/D). It shows that Houlsby et al. [13], Chenggen et al. [18] and Hirai [17] approaches have similar results due to the similarity of the considerations and equations parameters. Please note that in all calculations presented in Figure 2-11 the uplift capacity is deduced by the weight of the caisson, and in Chenggen et al. [18] approach, υ/k is assumed as 10^3. This graph shows the increase in capacity where the differential pressure was neglected.

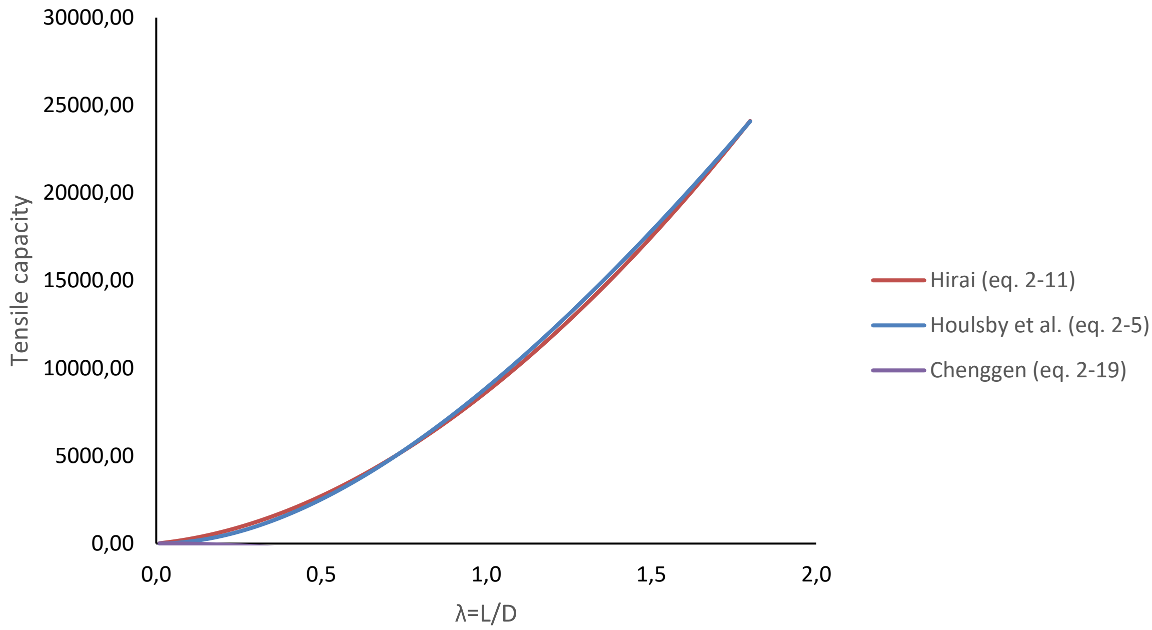

Figure 2-11 Comparison of methodologies for vertical tensile capacity

Comparing the resistance found with analytical and semi-empirical approaches presented in Figure 2-11, it was calculated with a simple equation of piles shaft friction resistance (eq. (2-19)).

$$V_{ult} = \gamma' K_0\, L^2\, D\, \pi\, tan\delta \tag{2-19}$$

In a comparison with Houlsby et al. [13] equation (2-3), both approaches have the same components to determine the friction resistance. Results presented in Figure 2-12 validates analytical (Houlsby et al. [13]) and semi-empirical (Hirai [17] and Chenggen et al. [18]) approaches by showing that frictional components applied in all approaches are the same and the results are similar.

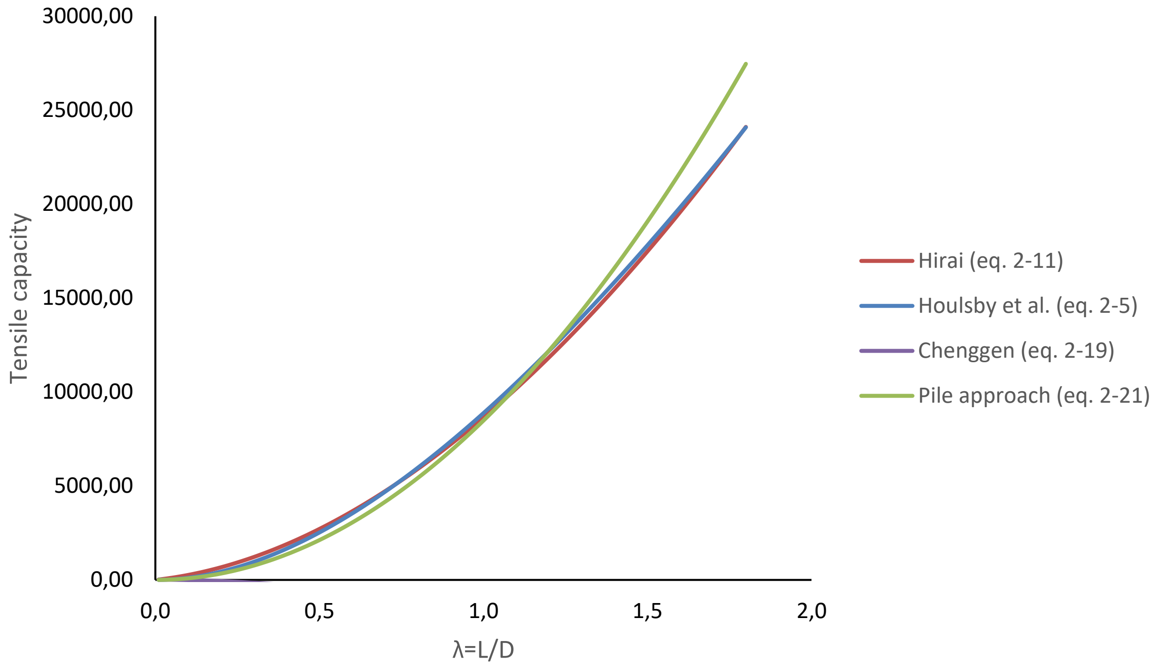

Figure 2-12 Comparison of pile friction resistance and other approaches

As Chenggen et al. [18] differential pressure influences directly in the vertical uplift capacity, and it is related with the pullout velocity υ/k, calculations were made to verify the influence of this parameter in the differential pressure and then in the vertical capacity. The results for the calculation for an aspect ratio of 1.5 are given in Table 2-1.

Table 2-1 Results of differential pressure and vertical capacity in function of υ/k

υ/k	f(υ/k)	g(L/D)	j(K,δ)	Do	γ' (kN/m^3)	p	Fv
1,00E-05	0,00	1,00	0,25	10,00	10,69	0,00	19041,92
1,00E-04	0,00	1,00	0,25	10,00	10,69	0,00	19041,95
1,00E-03	0,00	1,00	0,25	10,00	10,69	0,05	19042,29
1,00E-02	0,02	1,00	0,25	10,00	10,69	0,60	19046,65
1,00E-01	0,20	1,00	0,25	10,00	10,69	5,26	19083,26
1,00E+00	0,97	1,12	0,25	10,00	10,69	29,19	19271,20
1,00E+01	2,79	1,12	0,25	10,00	10,69	84,11	19702,49
1,00E+02	5,34	1,12	0,25	10,00	10,69	160,85	20305,23
1,00E+03	7,80	1,12	0,25	10,00	10,69	235,00	20887,60
1,00E+04	9,68	1,12	0,25	10,00	10,69	291,55	21331,75
1,00E+05	10,92	1,11	0,25	10,00	10,69	325,43	21597,82
1,00E+06	11,48	1,11	0,25	10,00	10,69	342,13	21728,97
1,00E+07	11,71	1,11	0,25	10,00	10,69	348,91	21782,25
1,00E+08	11,81	1,11	0,25	10,00	10,69	351,84	21805,24

Figure 2-13 shows the relation between the normalized pullout velocity in a range of 10^{-5} to 10^{8} and the differential pressure calculated. Figure 2-14 shows the relation for the vertical capacity.

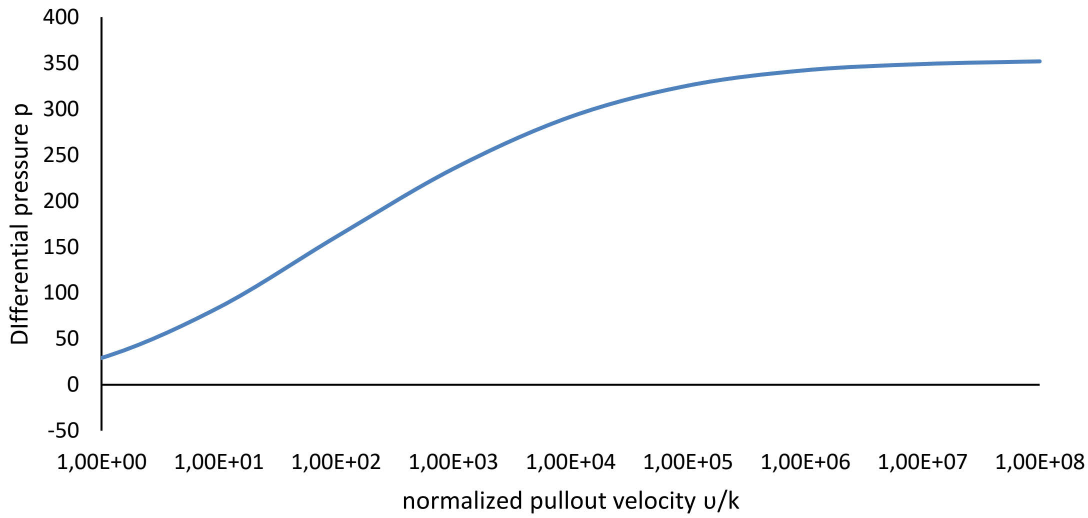

Figure 2-13 Relation between normalized pullout velocity and differential pressure

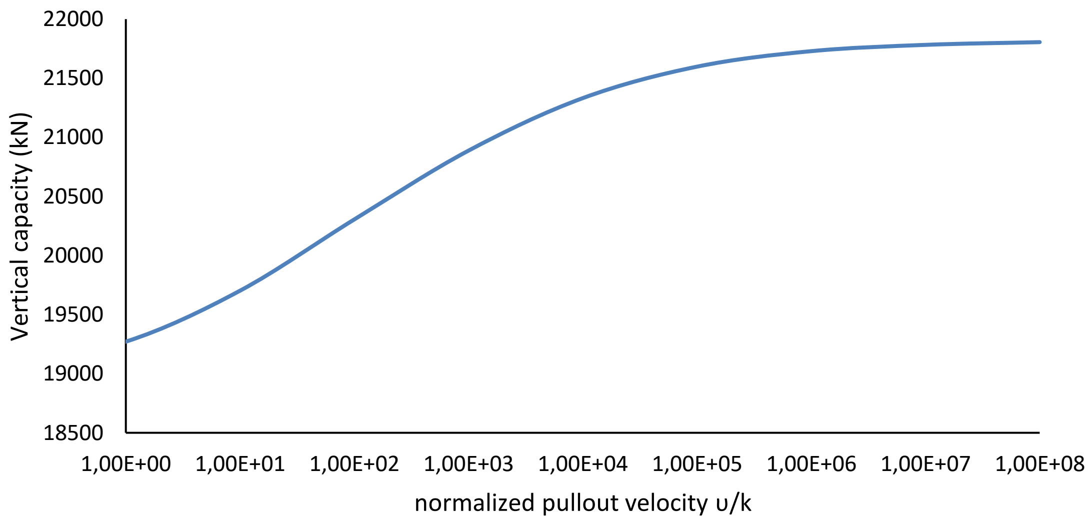

Figure 2-14 Relation between vertical capacity and normalized pullout velocity

As shown in the previous results, the normalized pullout velocity influences directly in the capacities in a relation that both differential pressure and vertical capacity grow significantly with the increase of the pullout velocity and around $\upsilon/k=10^{6}$ it starts stabilizing.

2.4.2 Design capacity under inclined load

Zhao et al. [16] analyses the uplift capacity of a suction caisson for floating structures with taut or catenary moorings that apply an inclined load on the caisson. The mobilized capacity is strongly dependent on the inclination of the load and the point of application of the load (centered or at the padeye as shown in Figure 2-15).

In his work, Zhao et al. [16] quantifies the capacity as a function of the combination of vertical, horizontal and moment loading acting on the caisson to develop yield envelopes. His work evaluates the drained capacity of a caisson subjected to an inclined load in a sandy soil in residual conditions. The soil dilatancy is ignored as strength is evaluated in terms of the critical-state friction angle ϕ_{cv}. This analysis is applicable to both loose or dense sands.

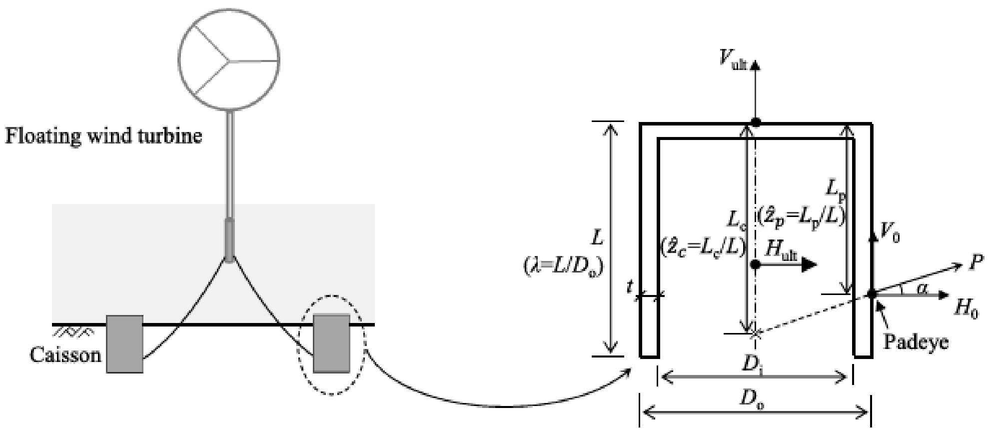

Figure 2-15. Floating wind turbine and notation for the caisson under inclined loading (Zhao et al. [16])

To determine the yield envelopes is necessary to calculate the ultimate horizontal and vertical capacity (H_{ult} and V_{ult}).

The horizontal capacity is determined by applying pure horizontal movement to the caisson to obtain translational displacements. It can be estimated empirically using the method for a rigid pile by integrating the limiting lateral resistance of the soil along the shaft (eq. (2-20)).

$$\frac{H_{ult}}{\gamma'^{D_o L^2}} = \frac{N}{2} \tag{2-20}$$

Where N is the lateral capacity factor ($2.3K_p\ k^{-0.165}$), which is a function of the soil stress level, k (k=γ' λ D_o /p_a).

The horizontal capacity at the padeye, H_0, is function of padeye depth (Zp) and associated caisson rotation as in equation (2-21).

$$\frac{H_0}{H_{ult}} = A\left(Z_p - Z_{H-opt}\right) + 1 \tag{2-21}$$

Where A is a bilinear function that depends on aspect ratio and normalized padeye depth (Zp) as follows in equations (2-22) and (2-23).

$$A = 1.04\lambda + 0.38\ \ for\ Z_p \leq Z_{H-opt} \tag{2-22}$$

$$A = -0.78\lambda - 0.06\ \ for\ Z_p \leq Z_{H-opt} \tag{2-23}$$

The pure tensile ultimate vertical capacity may be calculated by applying Houlsby et al. [13] solution V_{ult}=W+V_f. where W is the caisson submerged self-weight and V_f is the frictional resistance along the caisson-soil interface, expressed as equation (2-24).

$$V_f = \gamma'\pi\ (Ktan\delta_\mu)\left[D_o Z_o^2\left(e^{-L/Z_o} - 1 + \frac{L}{Z_o}\right) + D_i Z_i^2\left(e^{-L/Z_i} - 1 + \frac{L}{Z_i}\right)\right] \tag{2-24}$$

Where Z_o and Z_i are defined as equations (2-25) and (2-26).

$$Z_o = \frac{D_o(m^2 - 1)}{4(Ktan\delta)} \tag{2-25}$$

$$Z_i = \frac{D_i}{4(Ktan\delta)} \tag{2-26}$$

Where K is the lateral pressure coefficient equal to K_0=1-sin(ϕ), D_i is the internal diameter, m is the load-spreading parameter to account for vertical reduction in the soil outside the caisson (typically 1.5-2.0), δ is the interface friction angle.

The normalized ultimate vertical capacity increases approximately linearly with the stress level factor, k, according to equation (2-27).

$$\frac{V_{ult}}{W} = 0.73\ Ktan\delta\ \frac{pa}{\gamma_c'\ t}\ k + 1.0 \tag{2-27}$$

Where γ'_c is the caisson effective unit weight.

Then the horizontal capacity at the padeye, H_0, should be estimated. To identify the optimal normalized padeye depth for horizontal capacity (Z_{H-opt}), it's necessary to apply a horizontal displacement at the caisson, and the value changes with the aspect ratio of the caisson.

Zhao et al. [16] proposes a simple expression to determine the optimal normalized padeye depth for a given inclination load and caisson aspect ratio. The normalized depth where the load vector and the centerline of the caisson intersect Z_{c-opt} is given by the equations (2-28) and (2-29).

$$Z_{c-opt} = Z_{p-opt} + tan \propto/2\lambda \tag{2-28}$$

$$Z_{p-opt} = \eta e^{\eta-\alpha} \tag{2-29}$$

where α is the angle of the load inclination, λ is the slenderness of the caisson, and η=0.26λ+0.38.

The padeye depth Lp commonly used in design of suction caisson is 0.65L because of the lateral pressure on the skirt. The point of equilibrium is considered the point of application of the impulse in earth thrust theory, adopted 2/3h for the triangular diagram. Since Zp=Lp/L the normalized padeye depth Zp=0.65.

After having the ultimate capacities, it is possible to evaluate the yield envelopes by the equation (2-30).

$$\left(\frac{V}{V_0}\right)\left(1 - a\left(\frac{H}{H_0}\right) + b\left(\frac{H}{H_0}\right)^n\right) + \left(\frac{H}{H_0}\right)^2 = 1 \tag{2-30}$$

where a and b are function of normalized padeye depth, calculated as $a=1.22-1.12Z_p$, $b=0.39-0.97Z_p$ and n=4.7-2.39λ. The flowchart presented by Zhao et al. [16], Figure 2-16, summarizes the approach as described in this section.

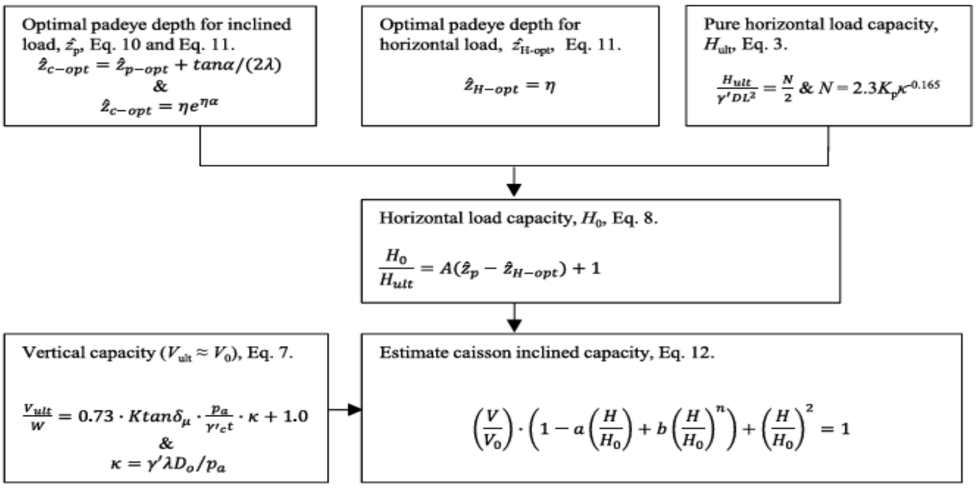

Figure 2-16. Calculation flowchart (Zhao et al. [16])

2.4.3 Material factors

DNV 119 [20] and 212 [21] recommend the application of a material factor to the characteristic resistance load, $R_c(Z_p)$, to obtain a conservative uplift capacity, $R_d(Z_p)$. For suction anchors the material factor applied is γ_m=1.2 for ultimate limit states (ULS) and γ_m=1.0 for accidental limit states (ALS), as expressed in equation (2-31).

$$R_d(Z_p) = \frac{R_c(Z_p)}{\gamma_m} \tag{2-31}$$

2.4.4 Cyclic loading

The soil behaviour under cyclic loading and repeated stress caused mainly by severe waves and storm loads is different from the one under monotonic loading. Cyclic loading generates excess pore pressures, reducing effective stress in the seabed and causing average and cyclic shear strains, leading to a loss of shear strength or stiffness of the seabed sediments.

The characterization of sand behaviour under cyclic loading will typically involve liquefaction assessment by estimating the magnitude of excess pore pressure, cyclic strains, and resulting displacements and permanent strains in the soil.

Cyclic shear strength ($\tau_{f,cy}$) is the peak stress that can be mobilized during cyclic loading, given by the equation (2-32).

$$\tau_{f,cy} = (\tau_a + \tau_{cy})_f \tag{2-32}$$

Where τ_a is the average shear stress and τ_{cy} is the cyclic shear stress as shown in Figure 4-6. The cyclic shear strength also depends on the type of test (simple shear or triaxial).

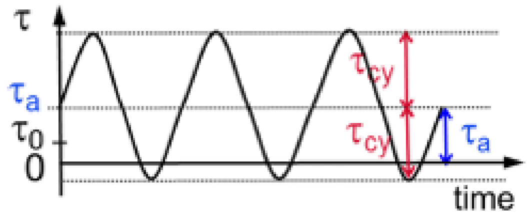

Figure 2-17 Cyclic and average shear stress in function of time [22]

To determine the cyclic shear strength of the soil, the contour diagram approach from Andersen [22] is one of the most used methodologies to evaluate the evolution of strains, pore pressures, and cyclic resistance under repeated loading conditions. Although the contour diagram approach was initially developed for clays, it can be also applied to sands [22].

The contour diagrams concept leads to the reduction of the monotonic capacity by defining the γ_{cy} for a certain equivalent number of cycles to failure, Neq, as function of the average shear stress, γ_a.

The soil strength is evaluated in the laboratory by determining the number of cycles to failure in direct simple shear (DSS) tests or triaxial tests as function of the average shear stress (τ_a) and cyclic shear stress (τ_{cy}) when a regular cyclic loading is applied. However, in real cyclic load histories the shear stress varies in each cycle so it's necessary to transform the irregular cycles into an equivalent number of cycles, Neq, with constant shear stress to estimate the same cyclic degradation as the actual irregular cyclic load history.

Both average shear stress (τ_a) and cyclic shear stress (τ_{cy}) are normalized by the vertical consolidation stress σ_{vc}. In the case of a suction anchor, σ_{vc} is calculated by the sum of the effective vertical stress of the soil, the weight of the caisson deduced by the buoyant weight, and the weight of the water above the caisson lid.

To determine the equivalent number of cycles the pore pressure accumulation procedure is adopted for undrained conditions. Considering a load time history corresponding to a possible storm at the design site, the loads are scaled for the maximum normalized cyclic shear stresses of $\tau_{cy,máx}/\sigma'_{vc}$ = 0.10, 0.15, 0.20 and 0.25. Then the pore pressure accumulation is evaluated in a pore pressure contour diagram representing the number of cycles with τ/σ'_{vc} to evaluate the permanent pore pressure and repeat the procedure for each parcel until Neq is found for the maximum shear stress.

This procedure is repeated for all scales to verify the variation of Neq due to the scaling factor as illustrated in Figure 2-18, taken from Andersen [22].

N	F/F_{max}	τ/σ_{vc}'	τ/σ_{vc}'	τ/σ_{vc}'	τ/σ_{vc}'
1	100	0.100	0.150	0.200	0.25
1	97.5	0.975	0.146	0.195	0.24
2	92.5	0.925	0.139	0.185	0.23
5	83	0.83	0.125	0.166	0.21
35	70	0.70	0.105	0.140	0.18
87	57	0.57	0.085	0.114	0.14
176	47.5	0.475	0.071	0.095	0.12
339	38	0.38	0.057	0.076	0.10
582	28	0.28	0.042	0.056	0.07

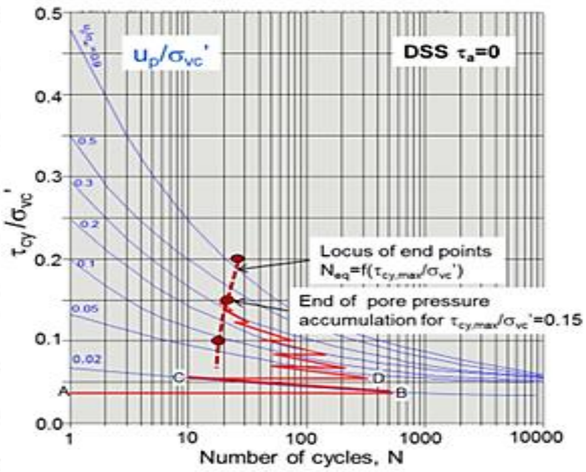

Figure 2-18 Pore pressure accumulation for undrained conditions in clays. (Andersen [22]). a) cyclic load composition table; b) pore pressure accumulation procedure.

With Neq determined, it is possible to determine the cyclic degradation rate using the contour diagram to plot the τ_a/σ'_{vc} (value must be between 0 and 1) of the load time series and the equivalent number of cycles to determine τ_{cy}/σ'_{vc}. The monotonic capacity is then factored by the τ_{cy}/σ'_{vc} value to determine the cyclic strength.

3
CASE STUDY DESCRIPTION

3.1 TAILWIND PROJECT STUDIED SCENARIOS

This work was based on the information compiled during TAILWIND European project (https://tailwind-project.eu/). This project funded by the European Union, is composed by international, multisectoral and multidisciplinary consortium focused on improving mooring and anchoring (station-keeping) technologies for floating offshore wind farms.

There are three reference locations in TAILWIND data. RL1 is a clayey soil in Utsira Nord in the North Sea, RL2 is a sandy soil in Provence Grand Large in the Mediterranean Sea, and RL3 is a case study site in the North Atlantic coast offshore Portugal that is still being investigated, so there are no information available yet. The data given in the TAILWIND documentation for the reference location RL2 (Provence Grand Large, Figure 3-1), describes a soil mainly granular, composed of sands of various densities, in depths of 100m.

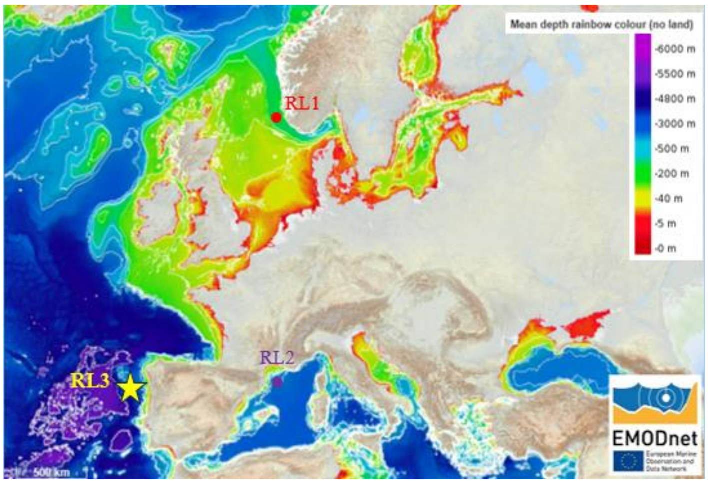

Figure 3-1 Reference location map [14]

Based on the information available in the public deliverables of the project, two scenarios were defined for the Golf of Lion where is expected to be a sandy soil: scenario 7 for semi-submersible floater and scenario 20c for TLP floater.

For scenario 20c, the TLP floater considered is a concrete TLP, symmetric about both vertical planes. It is supported by eight steel tendons that connect the floater and the suction caisson. The tension force along the tendons is always axial and the tendons play an important role in stabilizing the system against overturning (Figure 3-2) [15].

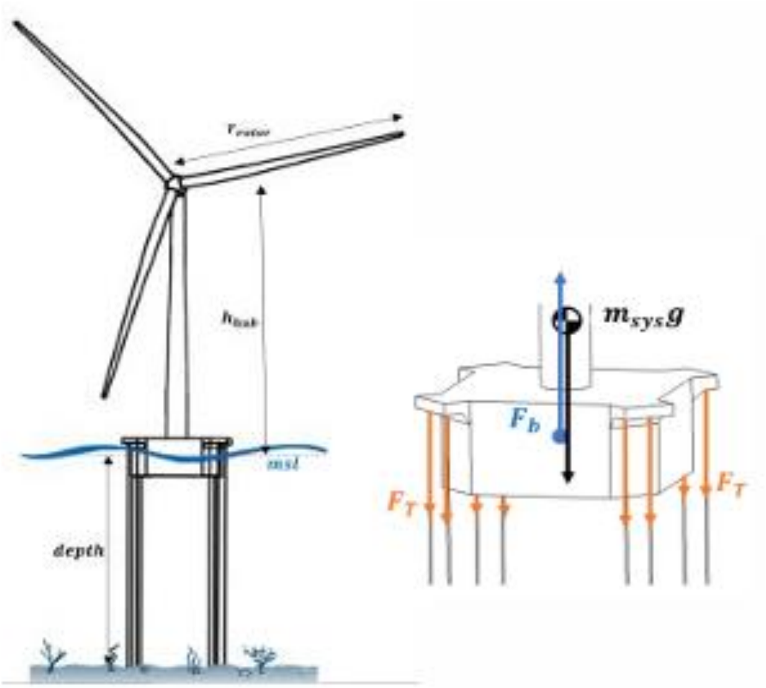

Figure 3-2 Scenario 20c mooring layout [15]

For Scenario 7, a semi-submersible floating platform with a semi-taut mooring system is considered, in which the mooring lines may develop a vertical load component under certain loading conditions. The floating structure adopted in the project consists of a quadrangular hull connected to a central column, which acts as a transition element for supporting the wind turbine tower. The mooring system is a hybrid semi-taut configuration composed of three main segments: an initial 50 m segment of 150 mm diameter R3S studless chain connected to the fairlead; a central 300 m segment of 258 mm diameter polyester fiber rope connected to a buoy to prevent its lower end from contacting the seabed; and a final 158 m segment of 150 mm diameter R3S studless chain connected to the foundation.

The stability of semi-submersible floating structures primarily depends on the ballast distributed within the four columns that form the platform. In contrast, the stability of Tension Leg Platforms (TLPs) relies on the tensile forces in the mooring tendons anchored to foundations on the seabed (Figure 3-3).

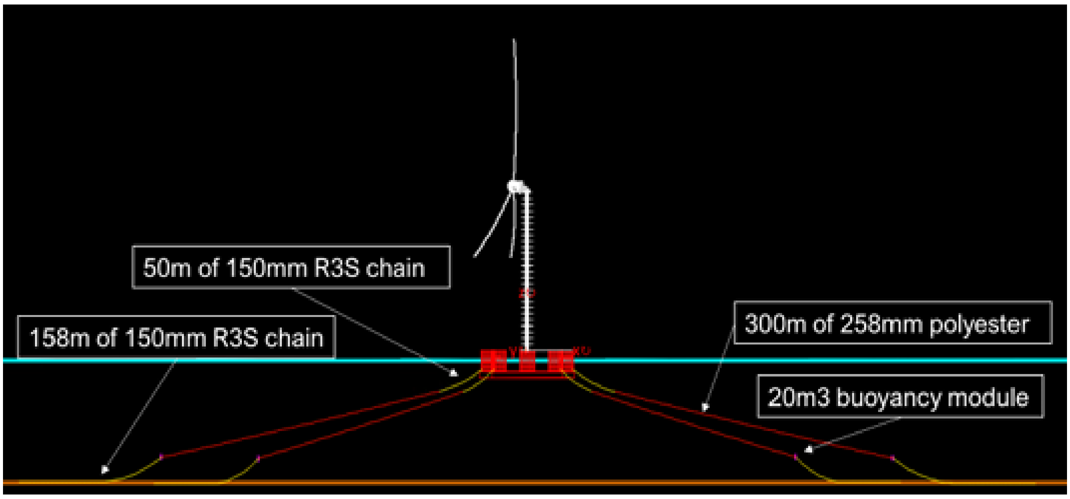

Figure 3-3 Scenario 7 semi-taut mooring layout [15]

The winds are predominant from northwest as shown in Figure 3-4. The wind intensity in this region generally generates low waves with periods of approximately 4–5 seconds; however, during storm events, wave heights may exceed 6 m.

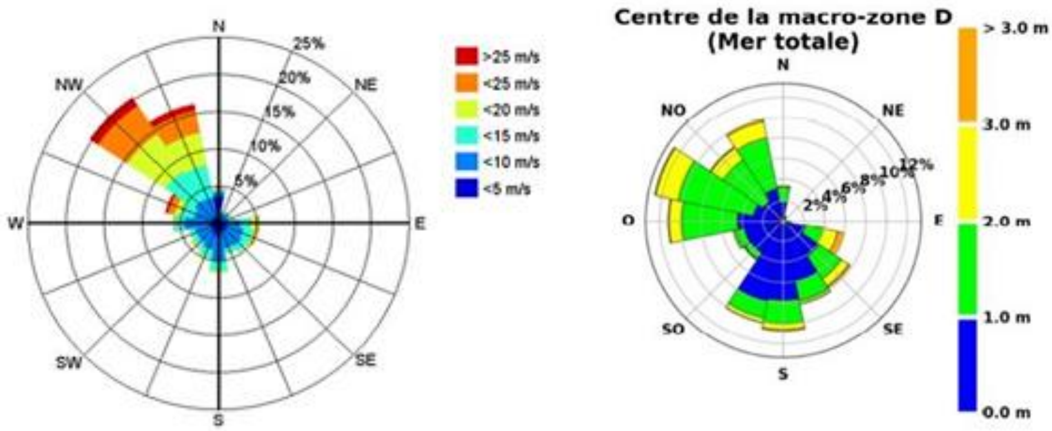

Figure 3-4. a) Wind rose of region RL2; b)Wind waves [14]

The most frequent waves in the region typically present peak periods ranging from 5 to 10 seconds, with wave heights of only a few tens of centimeters, rarely exceeding 1 m. Swell waves generated in distant seas may reach the region with heights of approximately 2 to 3 m during winter storms.

3.2 DESIGN TENSION LOADS

The hydrodynamic analysis performed in TAILWIND was based in several design load cases for each scenario with different combinations of metocean conditions. For each design load case, a load time series was obtained. Then the design tension load was obtained by applying load factors to the characteristic tensions as in equation (3-1).

$$T_d = \gamma_{mean}.T_{c,mean} + \gamma_{dyn}.T_{c,dyn} \tag{3-1}$$

where $T_{c,mean}$ is the characteristic mean tension, $T_{c,dyn}$ is the characteristic dynamic tension estimated, γ_{mean} is the tension load factor (permanent load), and γ_{dyn} is the dynamic tension load factor (environmental load). For semi-submersible structures were applied DNV [19] load factors of 1.3 and 1.75. For TLP structures were applied load factors of 1.0 and 1.3.

The design tension loads calculated as explained before for each selected scenario are decomposed in Table 3-1 to define the vertical and horizontal forces that are being applied to the suction caisson.

In TAILWIND [14], a new scenario was defined (scenario 20c), because scenario 20 resulted in a very large design load magnitude around 82.2MN. Understanding that this very high load resulted from a floating platform that was not optimized for the calculated scenarios, TAILWIND partners and stakeholders decided to design the TLP anchors for nominal design tension - presented in scenario 20c – adopting the API nominal stresses approach [23]. This consists in determining the stresses from member section properties and the resultant forces and moments from a global analysis at the member end.

Table 3-1. Summary of the load global analysis results

SUMMARY OF THE LOAD ANALYSIS RESULTS							
Platform	Site	Mooring concept	Scenario	Design Tension Td (MN)	Loading angle relative to horizontal (deg)	Decomposition (MN)	
Semi-submersible 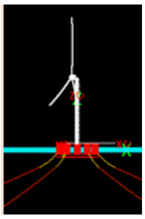	RL2 - Provence Grand large (100m)	Semi-taut	7	20,3	9,6	Td,v=	3,385
						Td,h=	20,016
TLP 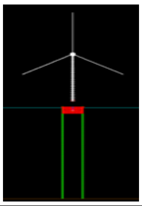	RL2 - Provence Grand large (100m)	Tendons	20c	17,6	90,0	Td,v=	17,600
						Td,h=	0,000

3.3 Geotechnical properties of the soil

The shear response of a soil depends on its void ratio and the normal effective and shear stresses acting on the soil mass. The definition of these effects depends on some parameters briefly discussed below.

The shear strength of uncemented sand is purely frictional, and its basic parameter is the coefficient of internal friction μ or the effective angle of shearing resistance ϕ. According to the Mohr-Coulomb failure criteria, the shear strength τ in a frictional material is function of the normal effective stress σ' on the failure plan (eq. (3-2)).

$$\mu = tan\phi = \frac{\tau}{\sigma'} \tag{3-2}$$

For saturated soils there are soil particles, and water, so the effective normal stress is the total stress reduced by the pore pressure u_w [1], $\sigma' = \sigma - u_w$.

When subjected to shearing the soil can dilate or contract and this behaviour is governed by the angle of dilation ψ, as shown in Figure 3-5.

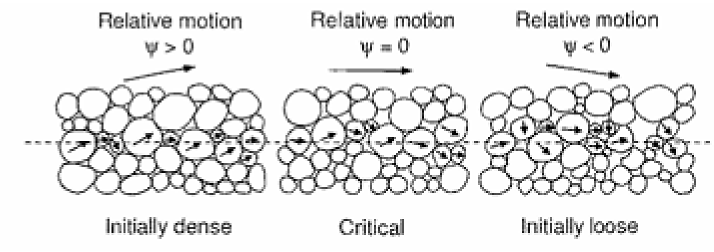

Figure 3-5. Dilation and contraction during shearing [1].

The maximum frictional resistance of a soil is mobilized when the angle of dilation is greatest, thus the peak friction angle ϕ_p (eq. (3-3)) is given by the sum of the critical state friction angle ϕ_{cs} and the dilation angle [1].

$$\phi_p = \phi_{cs} + 0.8\psi = \emptyset_{cs} + m[D_R(Q - \ln p') - R] \tag{3-3}$$

The tendency of soil to dilate or contract depends on the mean effective confining stress p' and the relative density, D_R. Q and R are intrinsic material parameters usually assumed 10 and 1 for clean sands, and m depends on the shear test (3 for triaxial and 5 for plane-strain) [1].

Reference Location 2, RL2, has a water depth of 100 m, and sandy soil at seabed. The geotechnical information about the seabed was based on CPT data from Gulf of Lion as shown in Figure 3-1. It consists of mainly medium dense to dense sand layers for which the main geotechnical properties are reported in Table 3-2, where γ is unit the weight of the soil, ϕ is the friction angle, q_t is the CPT cone resistance, D_r is the relative density and δ is the soil-interface friction angle.

Table 3-2. Soil properties of RL2

SOIL PROPERTIES						
Material	Depth z (m)	γ (kN/m^3)	ϕ(º)	q_t (MPa)	D_r (%)	δ (º)
Sand - Very loose to loose	0	20	28	0	35	29
	2	20	28	2	35	29
Sand - Medium to dense	2	20,5	33	10	70	29
	15	20,5	33	15	70	29
Sand - Very dense	15	21	37	20	90	29
	70	21	37	25	90	29

3.4 METHODOLOGY APPROACH

The suction caissons must withstand the static loads inherent to the suction anchors, as well as dynamic and cyclic loads caused by the metocean conditions such as waves and wind. The approach used to design the suction caissons was based on existing theories for the design of shallow and deep foundations extended to offshore environments.

From the sensibility analysis performed at 2.5.1.4 it was concluded that Hirai [17], Houlsby et al. [13], Chenggen et al. [18] approaches provide the same vertical capacity if the pullout velocity is small. Therefore, the research of Houlsby et al. [13] was considered, where the load capacity of the plate and the internal and external lateral resistances of the skirt are integrated to obtain the vertical resistance of the caisson. Houlsby et al. [13] analyses suction caisson under vertical loads only, so his methodology can be applied in scenario 20c, where the mooring is applied in the top center of the caisson with an angle of 90º.

For inclined loading, the research of Zhao et al. [16] considered the vertical and horizontal uplift capacity of the soil. Scenario 7 is a case of inclined load applied in the padeye. For this case Zhao et al. [16] methodology is applied to estimate the capacity of the suction caisson as function of the horizontal and vertical resistance to determine the yield envelope.

For the cyclic conditions in TLP scenario Andersen's [22] contour diagram methodology was adopted with some adaptations to the available data.

4
RESULTS

4.1 RESULTS FOR SCENARIO 20C

4.1.1 Sensitivity analysis

A couple of calculations were carried out to verify the influence of each parameter that governs the design capacity of the suction caisson, namely the slenderness or aspect ratio (λ=L/D) that is defined by the geometry, and the frictional parameter Ktanδ.

As illustrated in Figure 4-1, the vertical capacity increases with the slenderness ratio (L/D). This ratio has high influence in the vertical capacity due to the geometrical parameters L and D that influence the shaft frictional resistance forces.

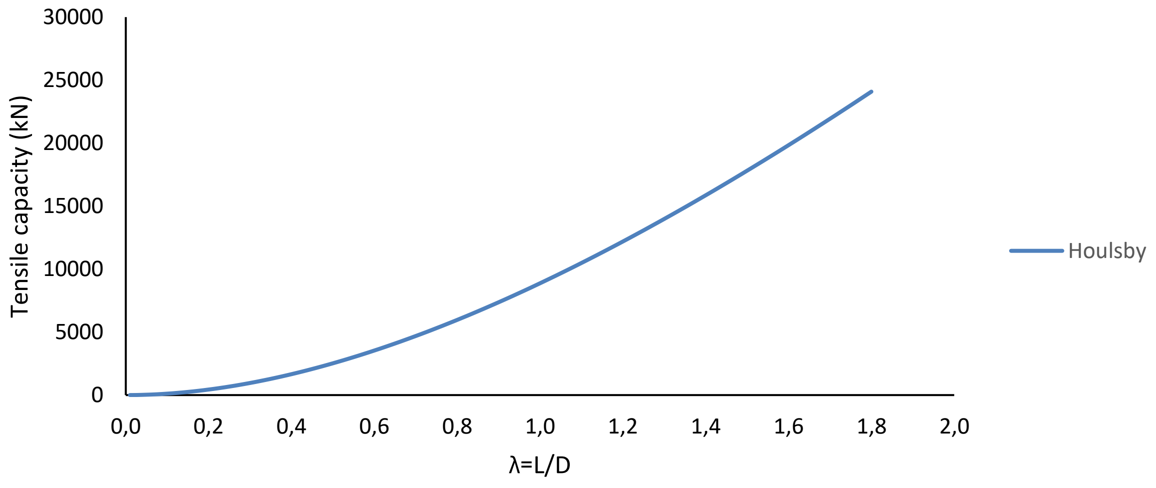

Figure 4-1 Houlsby et al. (eq. 2-10) vertical uplift capacity for different slenderness ratios

To evaluate the individual influence of the geometry parameters L and D, calculations were carried for two situations: first the same diameter was adopted for different lengths; and second the same length was adopted for different diameters.

For the first situation the diameters of Do=10m, Do=11m, and Do=12m were adopted, for skirt lengths that lead to the following slenderness ratios λ=0.5, λ=1.0, λ=1.5 and λ=2.0. The results can be observed in the graph of Figure 4-2, which shows that the vertical capacity increases with the slenderness.

For skirt length analysis, the calculations considered skirt lengths of L=15m, L=18m and L=20m, with diameters varying from Do=10m to Do=15m. The result presented in Figure 4-3 shows that the capacity increases linearly with the skirt length.

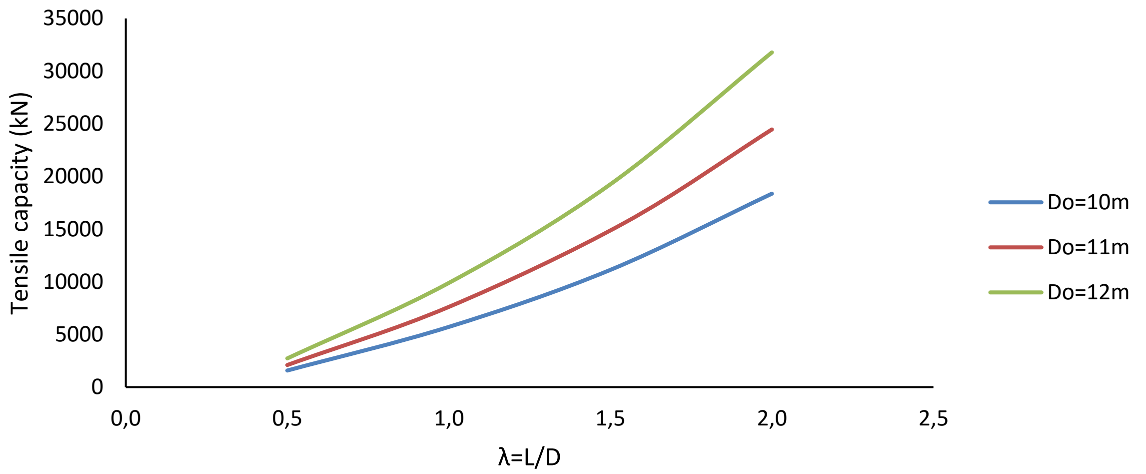

Figure 4-2 Caisson capacity in relation with the slenderness ratio for various caisson diameters

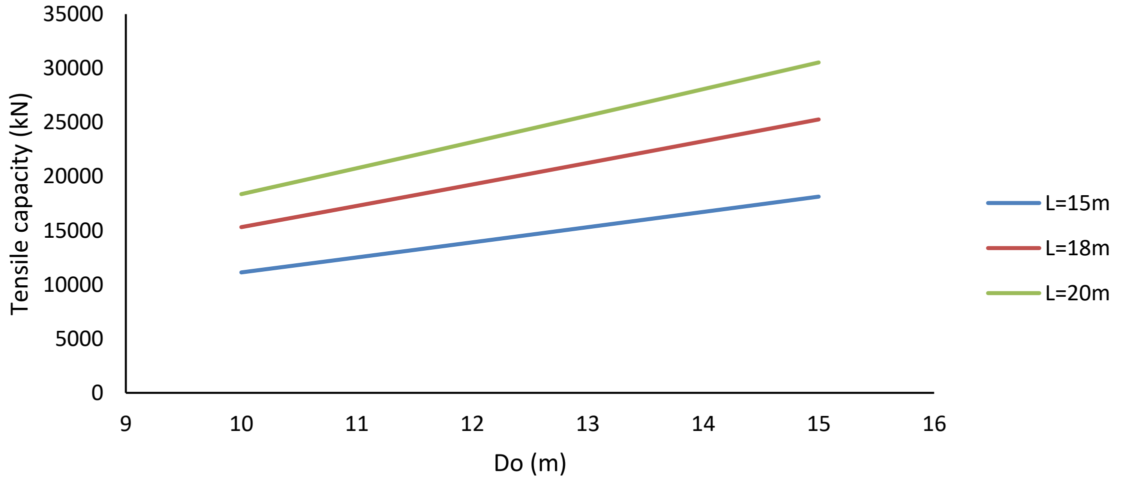

Figure 4-3 Caisson capacity in relation with the caisson diameter for various skirt lengths

To analyze the effect of the frictional parameters Ktanδ, the same calculations were made by defining a diameter Do=12m and a skirt length L=17m, with aspect ratio of λ=1.4. The values adopted for Ktanδ were 0.15 to 0.55 with increase of rate of 0.05. Figure 4-4 shows an almost linear relationship between the tensile capacity and the shaft friction parameter.

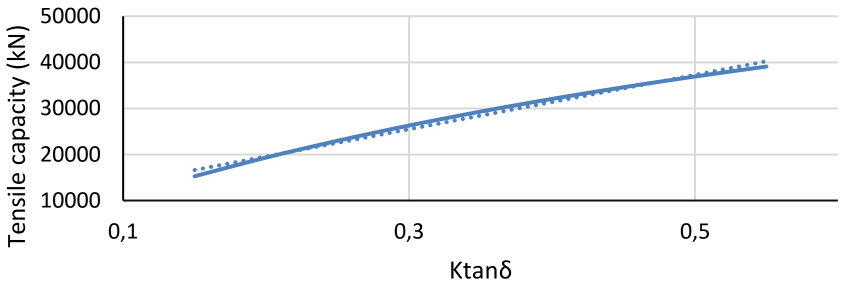

Figure 4-4 Caisson capacity in function of Ktanδ

4.1.2 Suction caisson design in monotonic conditions

The final geometry options considered for monotonic condition are given in the Table 4-1. For each caisson diameter, the skirt length was obtained so that the tensile capacity is equal to the design loads, taking into account the DNV [20] material factors of 1.2. It all cases, the following parameters were adopted Ktanδ= 0.35, ϕ=33º and δ=29º.

Table 4-1 Possible geometries of the caisson for scenario 20c

Do (m)	L (m)	h(m)	λ	Tensile capacity	Tr/Td
10,00	15,00	14,75	1,50	17892,70	1,02
11,00	14,00	13,75	1,27	17950,45	1,02
12,00	13,00	12,75	1,08	17617,80	1,00
13,00	13,00	12,00	1,00	17645,83	1,00
14,00	12,00	11,50	0,86	17888,89	1,02
15,00	11,00	11,00	0,73	17948,79	1,02

4.1.3 Suction caisson design in cyclic conditions

Considering the cyclic triaxial tests performed on Hokksund sand by FEUP team working on TAILWIND, it was concluded that Sand 3 contour diagram was the most similar. Since Hokksund sand has been used by the TAILWIND consortium to analyze the sand behaviour under cyclic loads it was considered herein for this design approach. Figure 4-5 shows the Sand 3 contour diagram plotting the obtained number of cycles to a shear stress of 10%. These results were obtained in cyclic triaxial tests where $\Delta\tau_a$,was applied in drained where the cyclic load τ_{cy} was applied in undrained conditions.

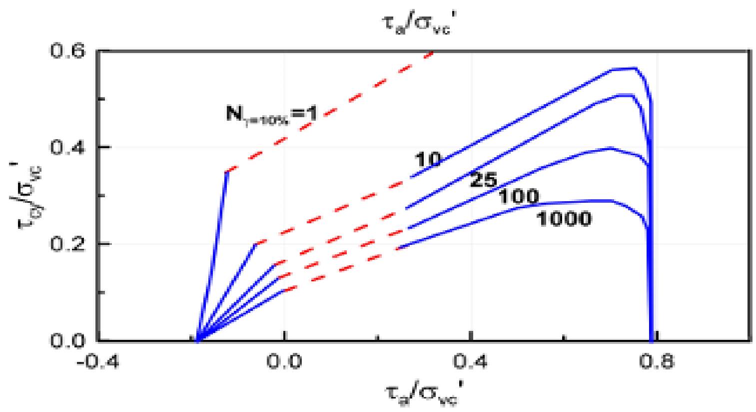

Figure 4-5 Contour diagram obtained in triaxial tests for sand 3: Dr≈65%; w=26%; σ'_{vc}=250kPa [22].

In the analysis carried out herein, it was not possible to determine the equivalent number of cycles associated to the storm due to lack of time. However, it was assumed that Neq varies between 10, 15 and 20 cycles. Therefore, the procedure described in the following assumed the average of these values.

The cyclic condition was estimated for scenario 20 since there was no hydrodynamic data available for scenario 20c. The analysis was carried out for twenty design load cases (DLCs) described in appendix A.1 for different metocean conditions that might act on the station-keeping system. For each DLC, TAILWIND hydrodynamic analysis provided a load time series of the padeye load for a possible storm. This data was analyzed to obtain the peak load for each anchor resulting in the tension design load presented in appendix A.2 for each DLC. Considering the maximum tension per anchor obtained in all DLC and considering that a TLP has 8 tendons this validates the design load of 82.2MN obtained for scenario 20.

The average and cyclic shear stresses (τ_a and τ_{cy}) were taken from the load time series of each DLC by defining the maximum and minimum force in the anchor and calculating the average shear stress and cyclic shear stress as described in section 2 ($\tau_{cy} = \tau_{max} - \tau_a$). Then these values were normalized by the vertical stress above the caisson lid calculated as described in section 2.5.4. Figure 4-6 shows the cyclic load history for anchor 1 - DLC 2 plotting the data for the first 1000 cycles.

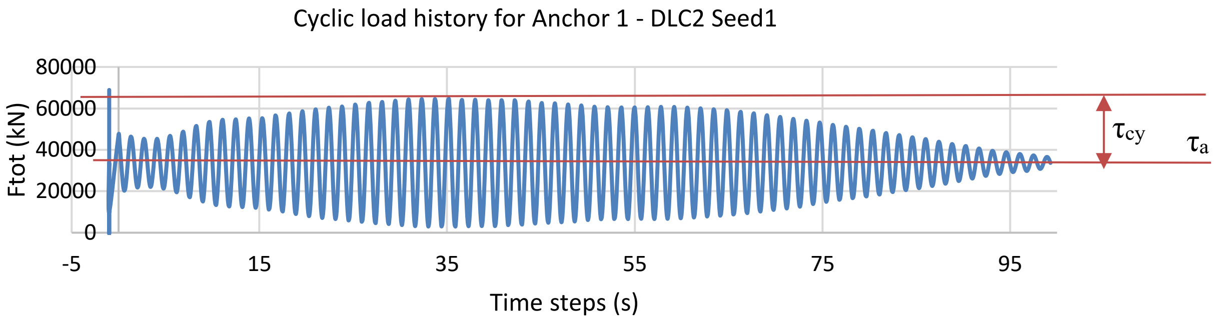

Figure 4-6 Example Cyclic load history for Anchor 1 - DLC 2 Seed1.

The results of the analyses for each DLCs are plotted in Table 4-2 representing the average and cyclic shear stresses for each anchor, as well as the vertical stress above the caisson lid and the normalized shear stresses that will be used in the contour diagram to define the number of cycles to failure of the caisson.

The normalized results for each DLC were plotted in a graph and overlayed in Andersen's [22] contour diagram obtained by performing triaxial tests on sand 3 to define the number of cycles to failure (Figure 4-7).

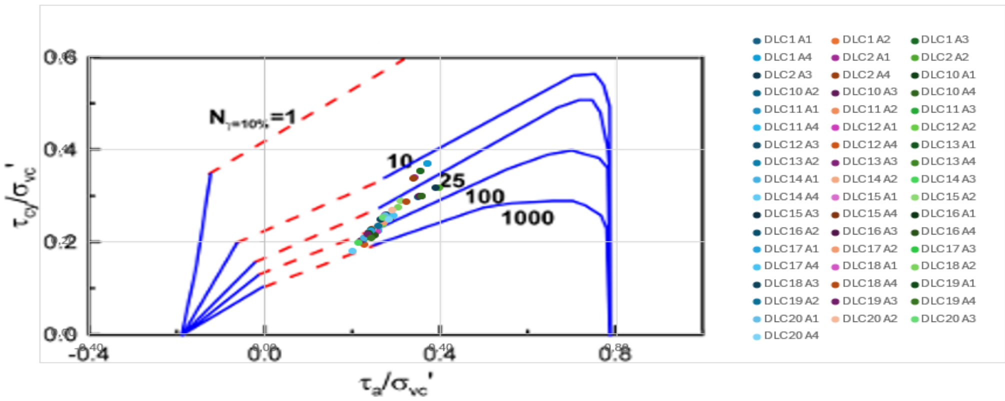

Figure 4-7 Plotted shear stresses overlayed Andersen's [22] contour diagram for sand 3

Table 4-2 Results for shear stress analyses (Do=10m; L=15m).

DLC	ANCHOR 1					ANCHOR 2					ANCHOR 3					ANCHOR 4				
	Ta (kPa)	Tcy (kPa)	σ'vo (kPa)	τa/ σ'vo	τcy/ σ'vo	Ta (kPa)	Tcy (kPa)	σ'vo (kPa)	τa/ σ'vo	τcy/ σ'vo	Ta (kPa)	Tcy (kPa)	σ'vo (kPa)	τa/ σ'vo	τcy/ σ'vo	Ta (kPa)	Tcy (kPa)	σ'vo (kPa)	τa/ σ'vo	τcy/ σ'vo
1	37659	37538	98909	0,38	0,38	35968	35890	98909	0,36	0,36	35951	35890	98909	0,36	0,36	37647	37519	98909	0,38	0,38
2	34527	34385	98909	0,35	0,35	40250	32054	98909	0,41	0,32	39538	32202	98909	0,40	0,33	34373	34276	98909	0,35	0,35
DLC3 to DLC9 have errors in hydrodynamic data																				
10	36341	30273	98909	0,37	0,31	35392	30121	98909	0,36	0,30	35707	30348	98909	0,36	0,31	36320	30278	98909	0,37	0,31
11	26213	22655	98909	0,27	0,23	25155	21769	98909	0,25	0,22	25274	21865	98909	0,26	0,22	26334	22755	98909	0,27	0,23
12	25867	22472	98909	0,26	0,23	27366	24179	98909	0,28	0,24	24588	21335	98909	0,25	0,22	23076	19615	98909	0,23	0,20
13	23005	21094	98909	0,23	0,21	22597	20716	98909	0,23	0,21	22198	20367	98909	0,22	0,21	23335	21350	98909	0,24	0,22
14	22916	21076	98909	0,23	0,21	24753	23019	98909	0,25	0,23	21758	19995	98909	0,22	0,20	20153	18265	98909	0,20	0,18
15	27946	26163	98909	0,28	0,26	31453	29370	98909	0,32	0,30	27743	25929	98909	0,28	0,26	29037	25332	98909	0,29	0,26
16	24607	22869	98909	0,25	0,23	28258	26180	98909	0,29	0,26	24088	22288	98909	0,24	0,23	25413	21719	98909	0,26	0,22
17	24597	22801	98909	0,25	0,23	27670	24478	98909	0,28	0,25	23949	22186	98909	0,24	0,22	29790	25965	98909	0,30	0,26
18	27543	25874	98909	0,28	0,26	30900	27782	98909	0,31	0,28	26879	25236	98909	0,27	0,26	32846	29103	98909	0,33	0,29
19	24094	22091	98909	0,24	0,22	26146	23816	98909	0,26	0,24	23825	21857	98909	0,24	0,22	24738	21111	98909	0,25	0,21
20	27846	26012	98909	0,28	0,26	29523	27305	98909	0,30	0,28	27453	25634	98909	0,28	0,26	28667	25141	98909	0,29	0,25

The DLCs that lay in between N=10 and N=20 were DCL1 and DLC2 anchors 1 and 4. They were considered the most critical because they led to a lower number of cycles to failure. The cyclic shear strength is estimated from this chart for each equivalent number of cycles using the average shear stress of DCL1 and DCL2. The reduction factor to be applied in the monotonic capacity to define the resisting tensile load under cyclic conditions is the normalized cyclic stress τcy/σ'vc.

As the effective stress of the soils varies with depth, each geometry has its own vertical effective stress and corresponding normalized stresses. For that reason, all the previous geometries were tested to verify the reduction factor for each case, and the results are available in appendix A.3.

The main results are summarized in Table 4-3.

Table 4-3 Cyclic shear stresses for Neq=10, Neq=15 and Neq=20

Geometry		Neq=10	Neq=15	Neq=20	τcy/σ'vo (%)
D (m)	L (m)				average
10	15	0,38	0,36	0,35	0,36
11	14	0,35	0,33	0,31	0,33
12	13	0,34	0,31	0,30	0,31
13	13	0,32	0,29	0,28	0,29
14	12	0,30	0,28	0,26	0,28
15	11	0,29	0,27	0,25	0,27

The tensile capacities defined for the monotonic condition calculated in section 4.1 and equation (2-3), and presented in table Table 4-1, were reduced by τ_{cy}/σ'_{vc} estimated in previous procedure. All geometries proved to be underdesigned and needed to be redesigned as shown in Table 4-4. If the diameter is kept constant the skirt length needs to be increased to take into account the cyclic loads.

Table 4-4 Tensile cyclic capacities for suction caisson geometries

Do (m)	L (m)	λ	Tensile monotonic capacity (kN)	τcy/ σ'vo (%)	Tensile cyclic capacity (kN)	Design Tensile load (kN)	Tr/Td
10	15	1,50	17892,70	36,00	11451,33	17600,00	0,65
11	14	1,27	17950,45	33,00	12026,80	17600,00	0,68
12	13	1,08	17617,80	31,00	12156,28	17600,00	0,69
13	13	1,00	17645,83	29,00	12528,54	17600,00	0,71
14	12	0,86	17888,89	28,00	12880,00	17600,00	0,73
15	11	0,73	17948,79	27,00	13102,62	17600,00	0,74

New geometries were calculated by applying the reductions of each tensile capacities to evaluate the effect of the cyclic response in the tensile capacities and design of suction caissons. As presented in Table 4-5 the increase in the slenderness ratio is proportional to the cyclic reduction factor. As higher $\tau_{cy}/\sigma'_{vc,}$ less vertical capacity so the geometry might be adapted to attend the resistance.

Table 4-5 Tensile cyclic capacities for suction caisson new geometries

Do (m)	L (m)	λ	Tensile cyclic capacity (kN)	Design Tensile load (kN)	Tr/Td
10	19	1,90	24394,28	17600,00	1,39
11	17	1,59	23890,03	17600,00	1,36
12	16	1,33	23186,16	17600,00	1,32
13	15	1,15	23130,21	17600,00	1,31
14	14	1,00	23306,21	17600,00	1,32
15	13	0,90	23259,72	17600,00	1,32

4.2 RESULTS FOR SCENARIO 7

4.2.1 Sensitivity analyses

To design the suction caisson for scenario 7 the calculations were made following Zhao et al. [16] approach. The first step is to define the normalized padeye depth Zp=Lp/L in function of the aspect ratio λ. In this case, the padeye depth, Lp, was calculated as 2/3 of the length L assuming an earth pressure triangular load, so that, Zp=0.65 as demonstrate in Figure 4-8. The calculations were carried for a couple of geometries but keeping the aspect ratio of always 1.5 and 1.0, and 0.5, and a constant Zp of 0.65.

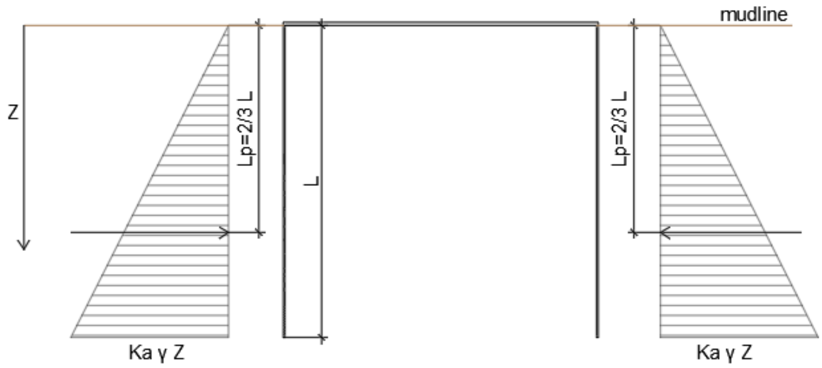

Figure 4-8 Diagram of Zp point of application

In these conditions, the yield envelope was defined following equation (2-30), where H is the horizontal component of the tension load and H_0 (eq. (2-21)) is the horizontal suction caisson capacity at the padeye, V is the vertical component of the tension load and V_0 is the vertical uplift capacity considered equal to the ultimate vertical capacity of the caisson V_{ult} (eq (2-24)).

Plotting vertical and horizontal results individually is possible to clarify the dependency of the capacities on the penetration depth. Vertical capacity (Figure 4-10) increases in depth due to the increase of the vertical effective stress once the main equation of the vertical capacity is the integral of $\sigma_v'\ (K tan\delta)(\pi D)dz$ [13]. The horizontal capacity (Figure 4-9) increases in depth when assuming soil depth Z equal to skirt length L to evaluate the required length to attend to the designing load.

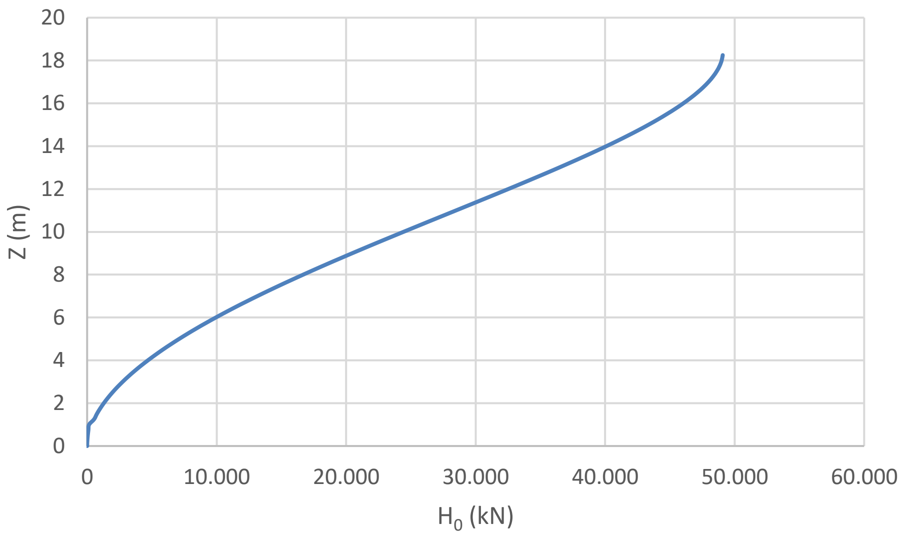

Figure 4-9 Horizontal capacity at padeye in function of the depth

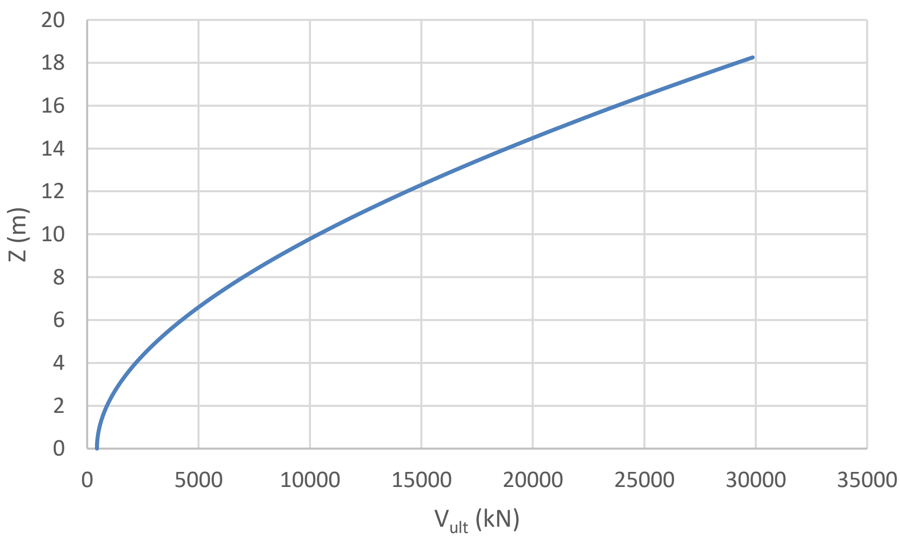

Figure 4-10 Vertical capacity at padeye in function of the depth

Assuming Do=10m, Ktanδ=0.35, ϕ=33º, δ=29º and an ascending L, the vertical and horizontal capacities in function of the soil depth, calculated using Zhao et al. [16] equations indicates an ascending value as the increase of the skirt length as represented in Figure 4-9 and Figure 4-10. The relation between V_{ult} and H_0 is given in Figure 4-11.

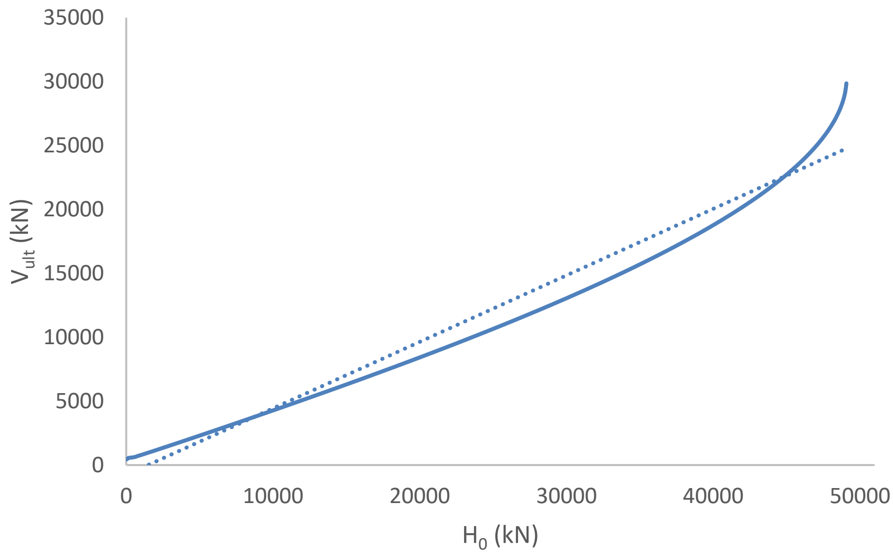

Figure 4-11 Vertical and horizontal capacities in function of soil depth

The envelope for vertical and horizontal capacities was calculated for different slenderness ratios, and it is possible to verify the influence of the slenderness in the capacity of the suction for the analysis with λ=0.5, λ=1.0 and λ=1.5 (Figure 4-12). The envelope analyses for each slenderness was taken by assuming H/H_0 values in a range 0-1 and then calculating the V/V_0 component with the equation (2-30).

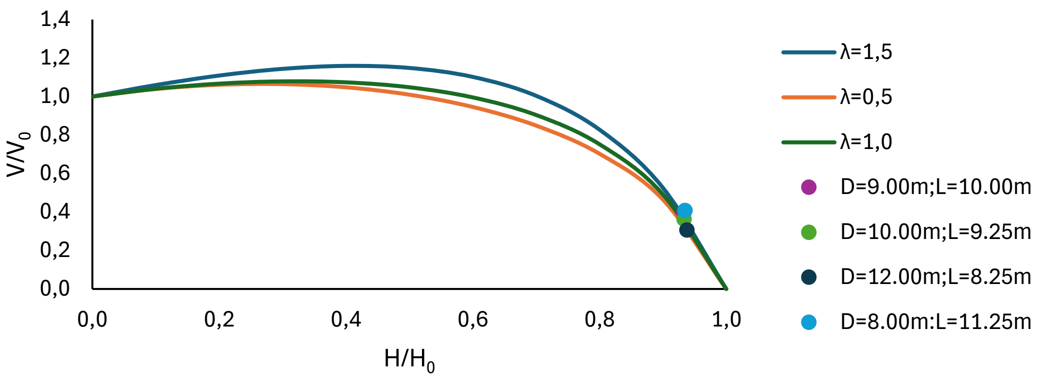

Figure 4-12 V-H normalized yield envelope for Zp=0.65.

Zp was also considered an important parameter in the design of the capacity, so it was studied the influence of different padeye depths to verify the influence of this parameter in the capacities for the aspect ratio of λ=1.5, and Zp=0.50, Zp=0.65 and Zp=0.80. The results are plotted in Figure 4-13 and it shows that as greater Zp, smaller are the capacities. The proximity of the padeye depth length Lp with the mudline increases slightly the capacities of the suction caisson since the increase of the capacities in the graph are not expressive. Therefore, it develops additional moment forces to the caisson, changing the behaviour of the caisson and its parameters for calculation. Also changing Zp develops different values for H_0.

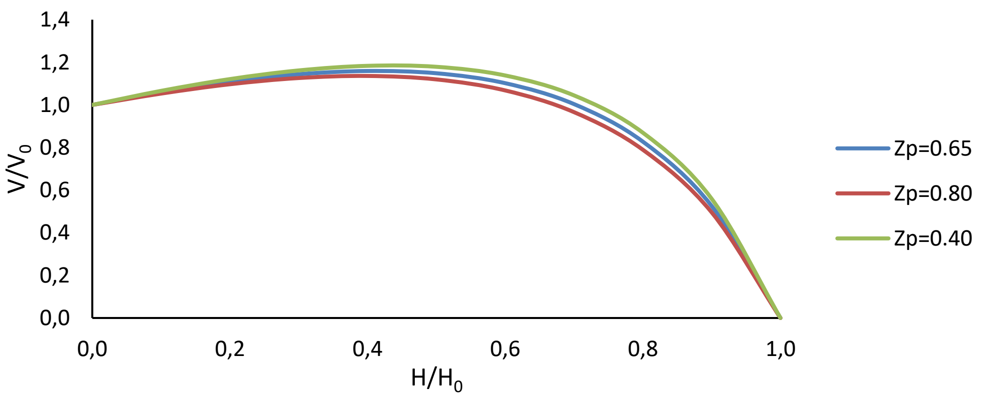

Figure 4-13 Influence of Zp in the caisson capacities

Comparing the failure envelope developed by Zhao et al. [16] with the failure envelope calculated in this section for λ=1.0 and Zp=0.65, it validates the calculation as the failure envelopes are identical. In Figure 4-14, *k* is the vertical effective stress level at the tip.

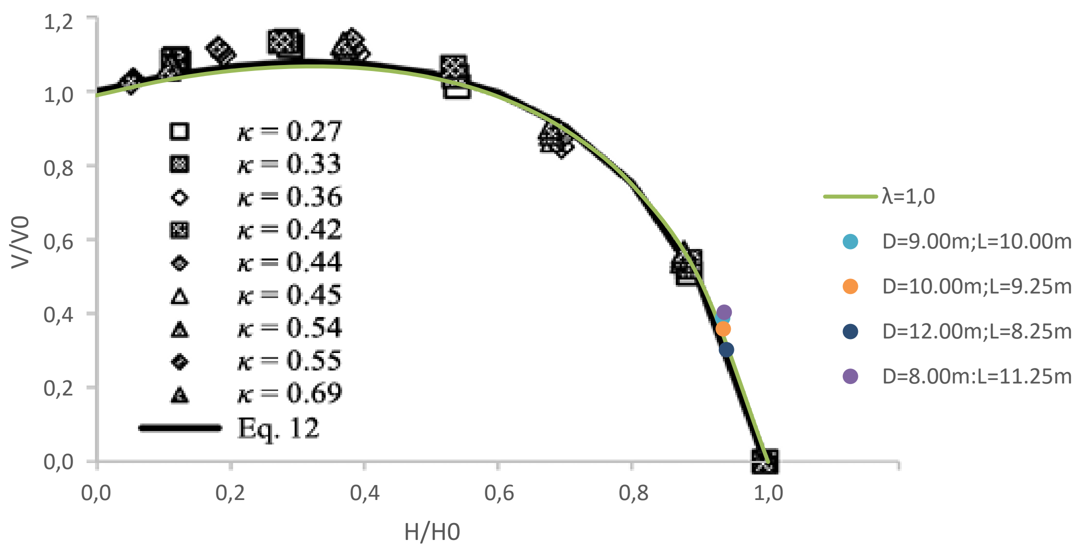

Figure 4-14 Comparison of Zhao et al. [16] and calculated failure envelopes

4.2.2 Suction caisson design

To equilibrate the design tensile load of 20.3MN at an angle of 9.6º, some geometries might be sufficient. The following parameters were considered: $K\tan\delta = 0.35$, $\phi=33^{\circ}$ and $\delta=29^{\circ}$. The allowable geometries calculated are in Table 4-6:

Table 4-6 Possible geometries of the caisson for scenario 7

Do (m)	L (m)	λ	V_{ult}	H_0	V/V_0	H/H_0	Envelope
8,00	11,25	1,41	8290	21412	0,408	0,935	0,624
9,00	10,00	1,11	8616	21464	0,393	0,933	0,694
10,00	9,25	0,93	9332	21442	0,363	0,933	0,714
12,00	8,25	0,69	11064	21338	0,306	0,938	0,658

The geometries presented in Table 4-6 are shown as markers in the envelope graph plotted in Figure 4-13. These results show that in caissons subjected to inclined loads for lower angles the main load to consider in resistance is the horizontal capacity. A small skirt depth is sufficient to attend scenario 7 vertical loads.

Comparing Table 4-6 and Table 4-1 it is observed that to attend inclined loads the geometry of the caisson can be smaller which may decrease the anchor cost. This is because the horizontal capacity is higher than the vertical capacities when comparing the same geometry.

In fact, when inclined loads are applied at the caissons at small angles to the mudline the main force is the horizontal component, moreover, applying the loads at the padeye also reduces anchor costs. Table 4-7 compares the anchor geometries when the loads are applied in the padeye and when the loads are applied at the center of the caisson.

Table 4-7 Comparison of the capacities of scenario 20c to the point of application of loads

	Loads applied on the top center of the caisson			Loads applied to the padeye of Zp=0,65		
Do (m)	L (m)	λ	Tensile capacity (kN)	L (m)	λ	Tensile capacity (kN)
10,00	15,00	1,50	17893	13,25	1,33	17851
11,00	14,00	1,27	17950	12,00	1,09	18246
12,00	13,00	1,08	17618	10,75	0,90	17908
13,00	13,00	1,00	17646	9,75	0,75	17682
14,00	12,00	0,86	17889	9,00	0,64	17790
15,00	11,00	0,73	17949	8,50	0,57	18459

Evaluating the influence of the inclination of the load for higher angles, assuming angles of 9.6º, 30º and 45º, and representing results in Table 4-8 is possible to conclude that changing the inclination of the load also changes the design loads components that must be supported by the caisson capacity. Increasing the inclination increases the vertical component that is achieved mainly by skirt penetration and then the skirt length must increase more than considering a lower inclination that solicitates mainly horizontal component. It was observed in the analysis that the horizontal capacity is higher than vertical capacity for same depth and that is the reason changing the load inclination in a way that vertical design load is the main stress demands higher slenderness ratio.

Table 4-8 Capacities for inclined loads in angles of 9.6º, 30º and 45º

	Load inclination of 9,6º				Load inclination of 30º				Load inclination of 45º			
Do (m)	L (m)	λ	V_0 (kN)	H_0 (kN)	L (m)	λ	V_0 (kN)	H_0 (kN)	L (m)	λ	V_0 (kN)	H_0 (kN)
10,00	9,00	0,90	8621	20464	10,00	1,00	10390	24430	12,25	1,23	14881	33521
11,00	8,50	0,77	9513	20552	9,00	0,82	10532	22731	10,75	0,98	14460	30813
12,00	8,00	0,67	10237	20183	8,00	0,67	10237	20183	9,75	0,81	14583	28737
13,00	7,75	0,60	11417	20659	7,50	0,58	10770	19454	9,00	0,69	14926	27112
14,00	7,50	0,54	12547	20943	7,00	0,50	11098	18437	8,25	0,59	14883	24954
15,00	7,25	0,48	13609	21057	6,75	0,45	11986	18442	7,50	0,50	14459	22421

The presented design solutions are quite different from those calculated in the TAILWIND project [14] due to the parameters and assumptions made. For instance, in scenario 20c, the suction anchor was designed in the TAILWIND project with substantial ballast to counterbalance the static vertical load. Ballast and drained external and internal skin friction resistance were designed to take the average part of the design tension. For this reason, the methodology followed herein provided much higher skirt lengths. For scenario 7, TAILWIND project assumed an anisotropic ratio between extension and compression cyclic shear strength of 0.6, which was not considered in the proposed work. For this reason, the proposed design suggests a lower skirt length than the TAILWIND project for this scenario.

5
CONSIDERATIONS AND FUTURE PERSPECTIVES

5.1 CONSIDERATIONS

This study aimed to design a suction caisson in sandy soil for offshore structures for two different floaters and load cases. The design was based on existing methods originally developed for clay conditions and adapted to sandy soils by analyzing laboratory centrifuge tests.

The results highlighted significant differences between existing analytical approaches, and the influence of each parameter particularly the angle of the application of the tension force, that governs the methodology and, consequently, the resistance capacity.

The study also showed that the geometry of the caisson plays a critical role in the overall resistance and performance of the anchor, but in both cases is the aspect ratio or the slenderness that governs the capacity of the caisson.

The frictional parameters are also critical to designing the suction caissons in granular soils since the vertical capacity is mainly computed by the sum of the frictional resistance components inside and outside the skirt of the caisson.

Under tension forces the lid contribute is neglectable and the resistance is given mainly by the friction in the walls and the submerged weight of the caisson, that apply a resistance force against uplift. Although the submerged weight of the caisson is not considered by Houlsby et al. [13] in the calculations of caisson under vertical tensile loads, it is considered by Zhao et al. [16] in his equations derived from Houlsby et al. [13] analytical works.

5.2 STUDY LIMITATIONS

Despite the insights obtained, the study is limited to using simplified analytical and semi-empirical models, without carrying out laboratory tests or finite element models to validate the results, which may not fully capture the complex soil-interface interaction and cyclic loading effects observed in offshore environments. Also, due to time limitation scenario 7 was not tested for cyclic loading.

5.3 RECOMENDATION FOR FUTURE WORKS

Future works should focus on the implementation of advanced numerical modelling techniques to better capture the nonlinear behaviour of sandy soils and the cyclic response of suction anchors. In addition, the effect of installation on the suction caisson capacity is also important since limited suction has to be applied to avoid soil liquefaction. Therefore, this subject should be studied in more detail.

REFERENCES

[1] Randolph, M., Gourvenec, S. Offshore Geotechnical Engineering. Spon Press, Abingdon, 2011.

[2] Bhattacharya, S. Design of Foundations for Offshore Wind Turbines. Wiley, Chichester, 2019.

[3] Abadie, C. N. Shared Anchor Pile Response to Multi-Directional Lateral Cyclic Loading. Proceeding of ISFOG, June 9-13, 2025, Gustave Eiffel University, Nantes.

[4] Sítio da internet https://www.utmconsultants.com/how-to-start-your-career-working-in-offshore-wind-farms/. 14/10/2025.

[5] Sítio da internet https://bluepowerpartners.com/grow-your-knowledge-on-floating-wind/. 16/10/2025.

[6] Torre, A., Tataki E., Ortolani C., Irvine J., McCall F., Fudge A., Hinxman D. Suction Caisson in Intermediate Soils. Conference paper, September 2023, Cathie.

[7] Chakrabarti, S. Handbook of Offshore Engineering. Elsevier, Oxford, 2005.

[8] ACES Technical Reference. Linear wave theory. Wave Theory.

[9] Chi-min Liu et al. On the study of Second-Order Wave Theory and Its Convergence for a Two-Fluid System. Mathematical Problems in Engineering, 19/03/2013, 12pg, Hindawi Publishing Corporation, Taiwan.

[10] ACES Technical Reference. Windspeed adjustment and wave growth. Wave Prediction.

[11] Villalobos, F. Installation of Suction Caissons in Sand. VI Congresso Chileno de Geotecnia, November 28-30 2007, Universidad Catolica de la Sma Concepción.

[12] Bai Y., Bai Q. Subsea Engineering Handbook. Elsevier, Oxford, 2010.

[13] Houlsby et al., G., Byrne, B, Kelly, R. The tensile capacity of suction caissons in sand under rapid loading. ISFOG, August 2005, 405-410pg, Taylor & Francis Group, London.

[14] Foglia, A., et al. Sustainable anchor concepts/D3.1. TAILWIND Project, 30/11/2024, 55pg.

[15] Foglia, A., et al. Project Design Basis/D1.1. TAILWIND Project, 31/12/2024, 76pg.

[16] Zhao et al., L., et al. Drained capacity of a suction caisson in sand under inclined loading. American Society of Civil Engineers, 2018, ASCE.

[17] Hirai, L., et al. Drained capacity of a suction caisson in sand under inclined loading. American Society of Civil Engineers, 2018, ASCE.

[18] Chenggen et al., X., et al. Calculation Method for Uplift Capacity of Suction Caisson in Sand Considering Different Drainage Conditions. MDPI, 2023, China.

[19] DNV. Support Structures for Wind Turbines (DNVGL-ST-0126); Det Norske Veritas: Bærum, Norway, 2018.

[20] DNV. Floating wind turbine structures (DNVGL-ST-0119), July 2018.

[21] DNV. Offshore soil mechanics and geotechnical engineering (DNVGL-RP-C212), august 2017.

[22] Andersen, K. H. *Cyclic soil parameters for offshore foundation design*. The third ISSMGE McClelland Lecturer (Frontiers in Offshore Geotechnics III– Meyer (Ed.)), 2015, Norwegian Geotechnical Institute, Oslo, Norway, 82p, Taylor & Francis Group (ISBN: 978-1-138-02848-7), London.

[23] API, 1997. Recommended Practice for Planning, Designing, and Constructing Tension Leg Platforms. In: IHS (Editor), API RP 2T.

[24] Pombo, J., Rodrigues, A., Silva, P. *Offshore Site Investigation of Sandy Sediments for Anchoring and Foundation Design of Renewable Energy Applications—NW Center of Portugal*. Marine Science and Engineering, 08/08/2025, 23p, MDPI.

[25] Fetter, C. W. Applied Hydrogeology. Prentice Hall, United States of America, 2001.

APPENDIX

A.1 DLCs DEFINITION FOR SCENARIO 20 (RL2)

ID	DLC	Reason proposed	Hub height wind speed (m/s)	Wind direction (deg)	Wave Sig. Height (m)	Wave peak period (s)	Wave direction	Current speed surf (cm/s)	Current direction	Water level (m)
1	1.1	Springing - just waves 1 m	0	0	1,00	3,00	COD	0,000	COD	-0,35
2	1.1	Springing - waves 1 m + thrust/current	max thrust	0	1,00	3,00	COD	0,833	COD	-0,35
3	1.1	Springing - just waves 2 m	0	0	2,00	4,50	COD	0,000	COD	-0,35
4	1.1	Springing - waves 2 m + thrust/current	max thrust	0	2,00	4,50	COD	0,833	COD	-0,35
5	1.6	MBL check	max thrust	0	7,50	8,00	COD	0,833	COD	1,25
6	1.6	Slack check	max thrust	0	7,50	8,00	COD	0,833	COD	-0,35
7	6.1	Slack check - wave centric	0	0	7,50	8,00	COD	0,980	COD	-0,35
8	6.1	MBL check - wave centric	0	0	7,50	8,00	COD	0,980	COD	1,25
9	6.1	Slack check - wind centric	38	0	7,50	8,00	COD	0,980	COD	-0,35
10	6.1	MBL check - wind centric	38	0	7,50	8,00	COD	0,980	COD	1,25
11	1.1	Springing - just waves 1 m	0	30 or 45	1,00	3,00	COD	0,000	COD	-0,35
12	1.1	Springing - waves 1 m + thrust/current	max thrust	30 or 45	1,00	3,00	COD	0,833	COD	-0,35
13	1.1	Springing - just waves 2 m	0	30 or 45	2,00	4,50	COD	0,000	COD	-0,35
14	1.1	Springing - waves 2 m + thrust/current	max thrust	30 or 45	2,00	4,50	COD	0,833	COD	-0,35
15	1.6	MBL check	max thrust	30 or 45	7,50	8,00	COD	0,833	COD	1,25
16	1.6	Slack check	max thrust	30 or 45	7,50	8,00	COD	0,833	COD	-0,35
17	6.1	Slack check - wave centric	0	30 or 45	7,50	8,00	COD	0,980	COD	-0,35
18	6.1	MBL check - wave centric	0	30 or 45	7,50	8,00	COD	0,980	COD	1,25
19	6.1	Slack check - wind centric	38	30 or 45	7,50	8,00	COD	0,980	COD	-0,35
20	6.1	MBL check - wind centric	38	30 or 45	7,50	8,00	COD	0,980	COD	1,25

A.2 PEAK LOAD RESULTS FOR EACH DESIGN LOAD CASES

	Td_L1_a Fairlead	Td_L1_b Fairlead	Td_L1_a Anchor	Td_L1_b Anchor	Td_L2_a Fairlead	Td_L2_b Fairlead	Td_L2_a Anchor	Td_L2_b Anchor	Td_L3_a Fairlead	Td_L3_b Fairlead	Td_L3_a Anchor	Td_L3_b Anchor	Td_L4_a_ Fairlead	Td_L4_b_ Fairlead	Td_L4_a_ Anchor	Td_L4_b_ Anchor
DC1	41489,11	41368,66	41184,60	41064,70	39558,53	39652,03	39249,24	39342,92	39534,00	39624,61	39224,65	39315,42	41472,24	41356,22	41167,70	41052,28
DC2	37961,21	37939,06	37653,92	37630,49	39358,61	39266,09	39040,28	38948,09	39082,02	38973,37	38763,95	38655,80	37899,24	37835,55	37593,86	37528,56
DC3	36044,08	35799,55	35713,93	35468,91	34628,36	34590,35	34296,18	34258,32	34603,41	34562,42	34271,18	34230,36	36032,76	35786,95	35702,57	35456,26
DC4	32804,76	32902,93	32474,27	32572,13	34925,93	34811,64	34590,61	34476,60	34651,02	34496,36	34315,12	34160,81	32573,32	32643,16	32242,82	32312,36
DC5	38669,73	38537,44	38330,48	38197,84	38335,68	38137,39	37995,58	37797,13	38235,21	38018,04	37895,22	37678,31	38344,53	38187,87	38002,54	37846,06
DC6	33586,40	33529,57	33242,51	33184,95	33332,43	33192,55	32987,05	32845,73	33201,88	33078,17	32855,19	32731,52	33329,95	33252,42	32985,74	32908,57
DC7	35464,93	35122,75	35118,79	34776,27	33372,80	33238,39	33026,07	32892,08	33362,15	33225,39	33015,41	32879,06	35453,15	35109,66	35107,00	34763,17
DC8	39154,29	38824,90	38807,99	38478,36	36737,98	36619,42	36392,72	36274,39	36723,83	36603,83	36378,65	36258,77	39140,85	38809,99	38794,52	38463,43
DC9	34353,78	34254,57	34013,86	33914,33	33561,64	33515,77	33217,56	33171,82	33642,00	33533,63	33298,03	33189,59	34143,24	34030,23	33803,70	33689,41
DC10	38450,20	38354,71	38110,44	38016,39	37884,12	37763,50	37544,27	37422,23	38115,80	37992,92	37776,24	37653,24	38316,88	38221,97	37978,12	37882,42
DC11	25787,24	25726,85	25422,43	25362,12	24705,06	24759,01	24339,20	24393,22	24824,47	24893,40	24458,82	24527,77	25912,63	25866,74	25548,07	25502,15
DC12	25258,25	25504,39	24891,34	25137,47	26889,55	26963,62	26521,20	26595,36	24272,70	24027,91	23904,99	23660,36	22621,71	22552,01	22255,45	22185,73
DC13	23037,63	23059,48	22662,62	22684,46	22734,33	22786,08	22358,52	22410,34	22218,19	22302,63	21842,74	21926,99	23433,83	23390,17	23058,42	23014,73
DC14	22809,07	23059,51	22432,81	22683,05	24798,01	24859,02	24421,13	24482,16	21934,88	21658,00	21558,19	21281,25	20223,39	20156,60	19847,06	19780,33
DC15	29015,36	28933,66	28633,90	28553,45	32495,26	32530,53	32115,63	32150,93	28558,66	28635,79	28177,84	28255,88	30277,93	30249,81	29897,71	29869,62
DC16	24978,74	24918,00	24597,52	24537,10	28391,09	28432,87	28009,75	28051,53	24687,51	24750,79	24306,35	24369,95	26147,80	26129,54	25764,19	25745,96
DC17	24900,77	24905,13	24520,96	24525,55	29048,68	29066,95	28666,03	28685,62	24211,81	24252,18	23830,59	23870,78	30300,63	30247,69	29917,13	29864,21
DC18	28689,57	28792,72	28307,65	28411,33	32713,37	32736,52	32332,11	32355,26	28163,95	28130,49	27782,06	27749,84	34499,30	34444,61	34117,99	34063,24
DC19	24932,18	24909,47	24552,56	24528,29	26765,49	26743,94	26384,23	26362,67	24498,88	24472,92	24117,61	24092,31	25759,35	25681,09	25377,40	25299,10
DC20	28686,38	28640,01	28306,85	28259,30	30661,99	30638,47	30283,06	30259,03	28062,65	28059,05	27678,71	27676,06	29425,17	29365,23	29046,63	28986,18
	41489,11	41368,65	41184,59	41064,69	39558,52	39652,03	39249,24	39342,91	39534,00	39624,60	39224,65	39315,41	41472,24	41356,22	41167,70	41052,28

A.3 PLOTTED SHEAR STRESSES AND NUMBER OF CYCLES TO FAILURE

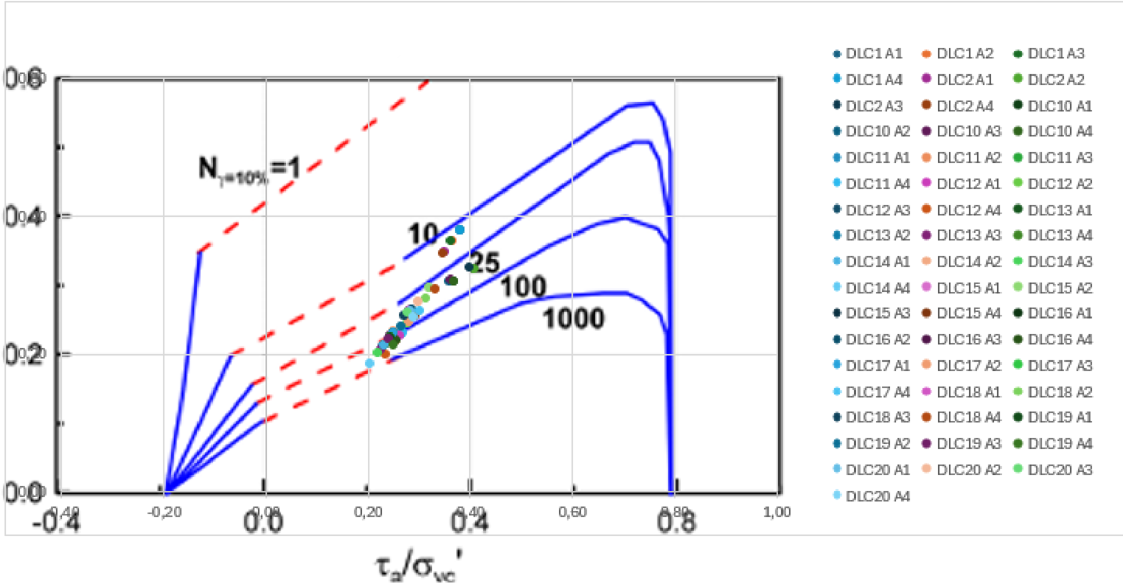

Figure 5-1 Shear stresses and number of cycles D=10m; L=15m

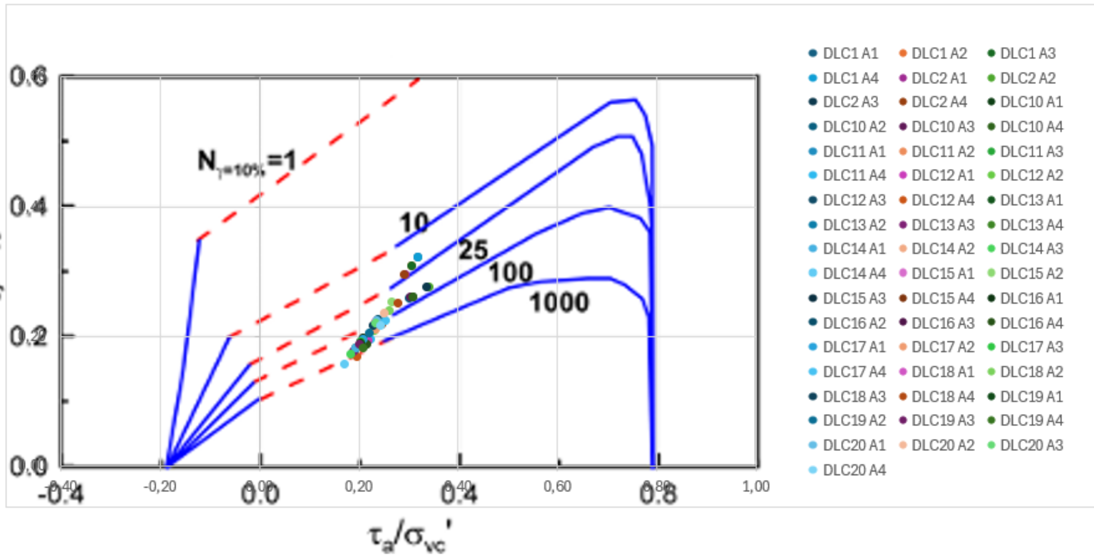

Figure 5-2 Shear stresses and number of cycles D=11m; L=14m

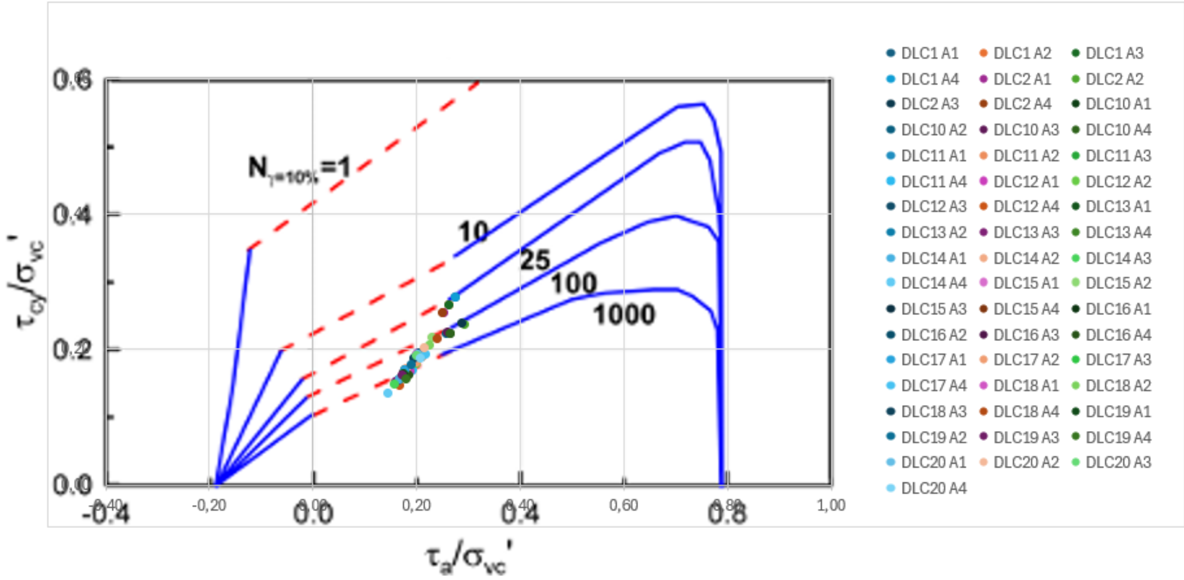

Figure 5-3 Shear stresses and number of cycles D=12m; L=13m

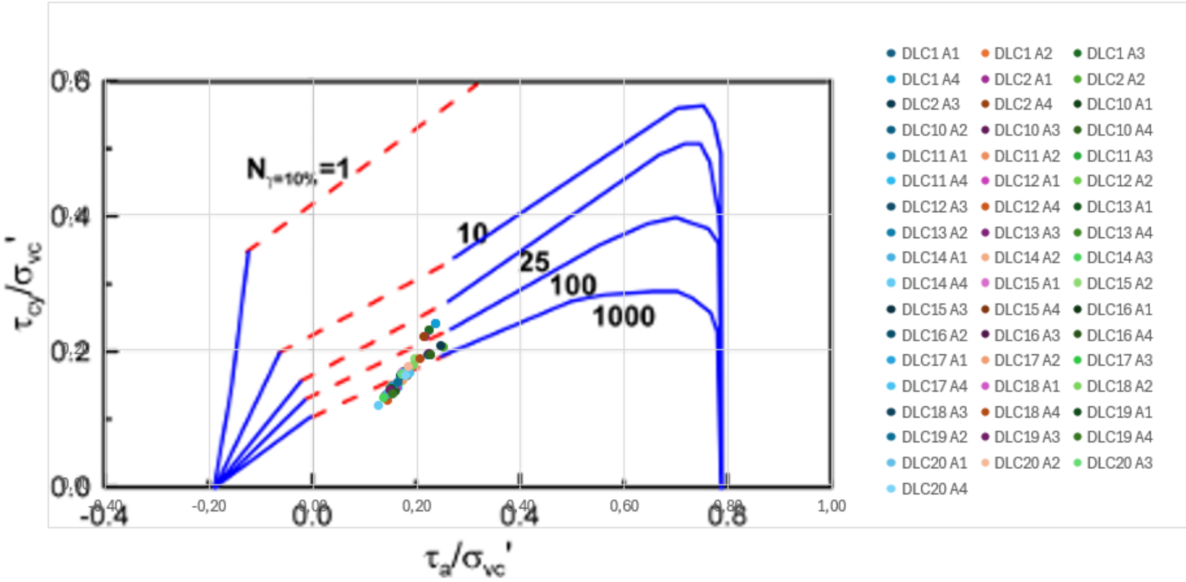

Figure 5-4 Shear stresses and number of cycles D=13m; L=13m

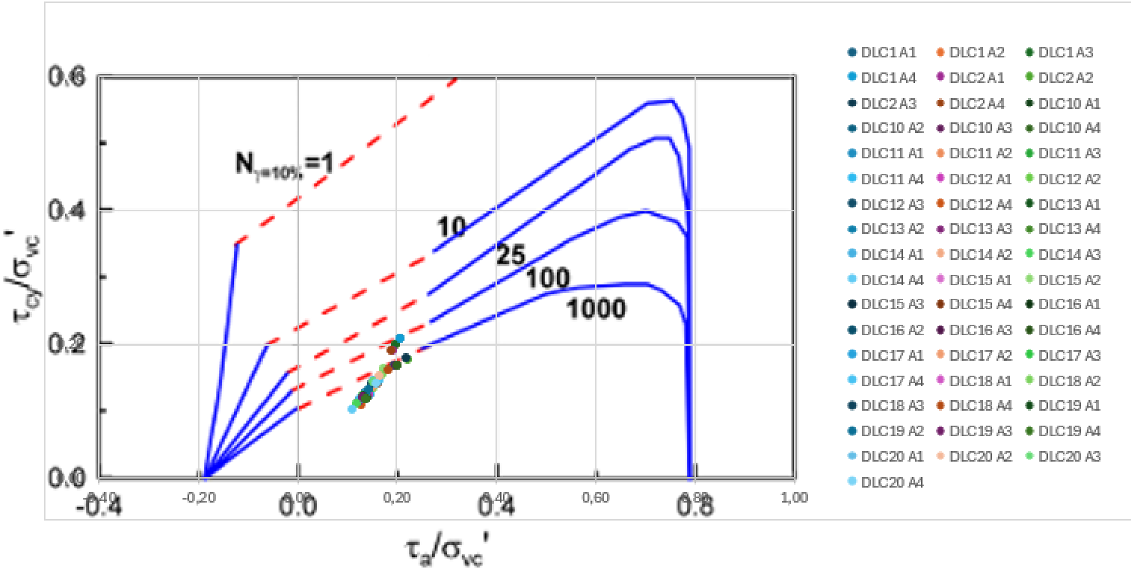

Figure 5-5 Shear stresses and number of cycles D=14m; L=12m

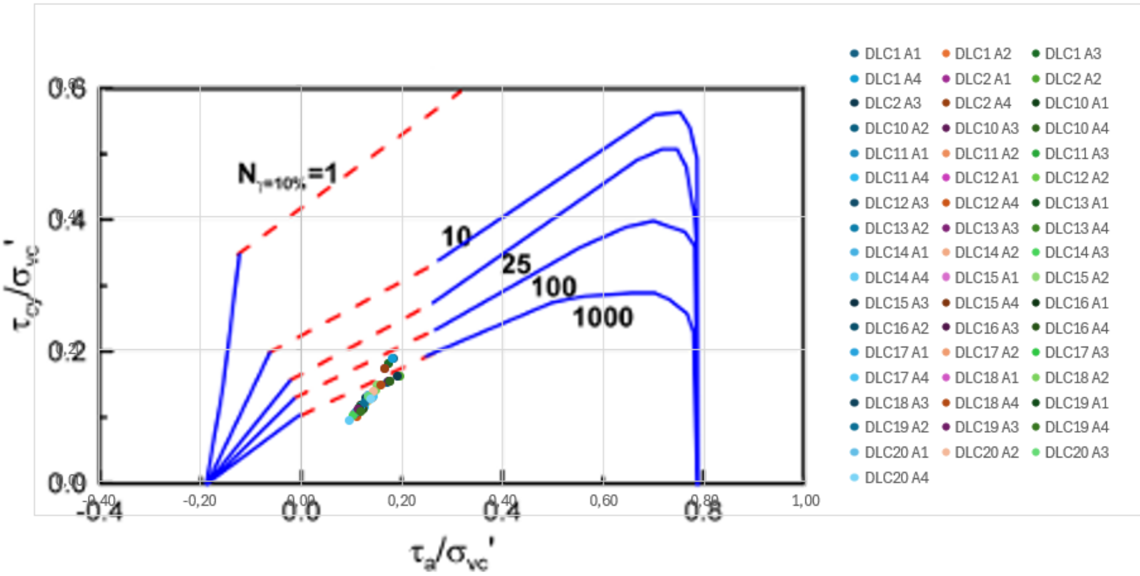

Figure 5-6 Shear stresses and number of cycles D=15m; L=14.25m